Inorganic Chemistry

pubs.acs.org/IC Article

Systematic Investigation of Coordination Chemistry in Iridium(III) and Ruthenium(II) Complexes Derived from Pyridyl−Amine Ligands and Their Anticancer Evaluation

Lihua Guo,* Zhihao Yang, Heqian Dong, Kangning Lai, Hanxiu Fu, Yuwen Gong, Susu Li, Mingbo Yue, and Zhe Liu*

Cite This: *Inorg. Chem.* 2025, 64, 10379−10401 Read Online

ACCESS | Metrics & More | Article Recommendations | Supporting Information

ABSTRACT: A systematic investigation of the coordination chemistry of iridium(III) and ruthenium(II) complexes synthesized from pyridyl−amine ligands was performed, focusing on how ligand steric hindrance and metal centers affect oxidation behavior, coordination modes, and biological activities. The study revealed that steric hindrance at the ligand's bridge carbon strongly influenced both oxidation behavior and coordination modes. Smaller substituents (e.g., H and Me) facilitated oxidation to form pyridyl−imine species under adventitious oxygen, whereas bulky substituents (e.g., *i*-Bu and mesityl) suppressed oxidation, yielding stable pyridyl−amine or 16-electron pyridyl−amido complexes. Moreover, iridium(III) complexes were more prone to oxidation than the corresponding ruthenium(II) complexes under similar conditions. The aqueous stability of the newly synthesized complexes was confirmed. Cytotoxicity assays demonstrated that most of the complexes exhibited notable anticancer potency against A549, HeLa and cisplatin-resistant A549/DDP cancer cells. Mechanistic studies suggested a redox-driven pathway involving the catalytic oxidation of NADH to NAD^+, the elevation of ROS levels and depolarization of the mitochondrial membrane. Notably, pyridyl−amine complexes induced apoptosis, while 16-electron pyridyl−amido complexes did not, though both caused S phase cell cycle arrest. Additionally these complexes can inhibit A549 cell migration, suggesting their potential to reduce cancer metastasis.

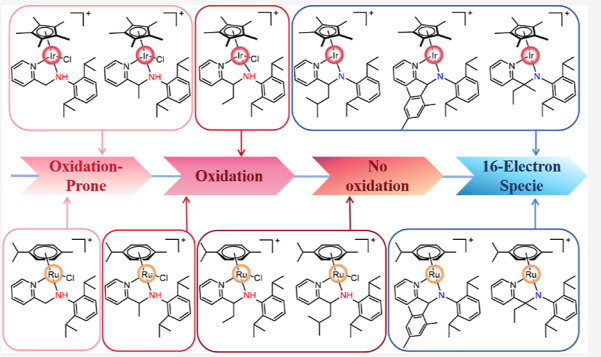

1. INTRODUCTION

Platinum-based anticancer drugs have been highly effective in treating various tumors.[1−6] Nonetheless, issues such as side effects and drug resistance have driven the search for alternative metal-based therapies. Among these, half-sandwich organometallic complexes of platinum group metals (e.g., iridium, ruthenium, osmium and rhodium) with piano-stool geometries have gained significant attention as potential anticancer agents.[7−13] These complexes have shown significant anticancer potential, operating through mechanisms of action (MoAs) that differ from those of platinum-based drugs. Research has primarily centered on exploring and investigating the 18-electron neutral and cationic complexes containing diverse bidentate XY chelating ligands.[13,14] Among these, *N*,*N*-donor ligands have been predominantly utilized.[15−39] A notable example is RM175, an arene−ruthenium(II) complex with an ethylenediamine (en) ligand (Scheme 1, **I**), which has demonstrated considerable cytotoxicity in vitro and in vivo.[40] Our group has observed that cationic half-sandwich pyridyl−imine iridium(III) and ruthenium(II) complexes generate substantial reactive oxygen species (ROS), disrupt mitochondrial membranes, and exhibit significant anticancer effects against A549 cancer cells (Scheme 1, **II** and **III**).[41−43] Certain ruthenium(II) complexes selectively targeted lysosomes and demonstrated high selectivity for A549 cancer cells over BEAS-2B normal cells.[42,43] Additionally, iridium(III) and ruthenium(II) complexes featuring α-diimine *N*,*N*-chelating ligands were synthesized (Scheme 1, **IV** and **V**). These complexes overcome cisplatin resistance by initiating apoptosis through ROS-related mechanisms.[44−46]

The aforementioned *N*,*N*-chelating complexes can be categorized into amine (sp^3-N/sp^3-N)-metal (Scheme 1, **I**) and imine (sp^2-N/sp^2-N)-metal (Scheme 1, **II**−**V**) coordination modes. With this basis, we further investigated hybrid sp^3-N/sp^2-N chelating complexes. It was observed that sp^2-N/sp^3-N pyridyl−amine complexes (Scheme 1, **VI**) could undergo oxidation to form pyridyl−imine iridium(III) complexes (Scheme 1, **VII**) in the presence of trace molecular oxygen.[47]

Received: December 31, 2024
Revised: March 18, 2025
Accepted: May 13, 2025
Published: May 17, 2025

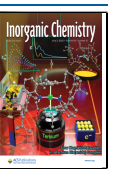

https://doi.org/10.1021/acs.inorgchem.4c05599
Inorg. Chem. 2025, 64, 10379−10401

Scheme 1. Reported Organometallic *N,N*-Chelating Half-Sandwich Platinum-Group Metal Complexes, Along with the Hybrid Coordination Modes Investigated in This Work

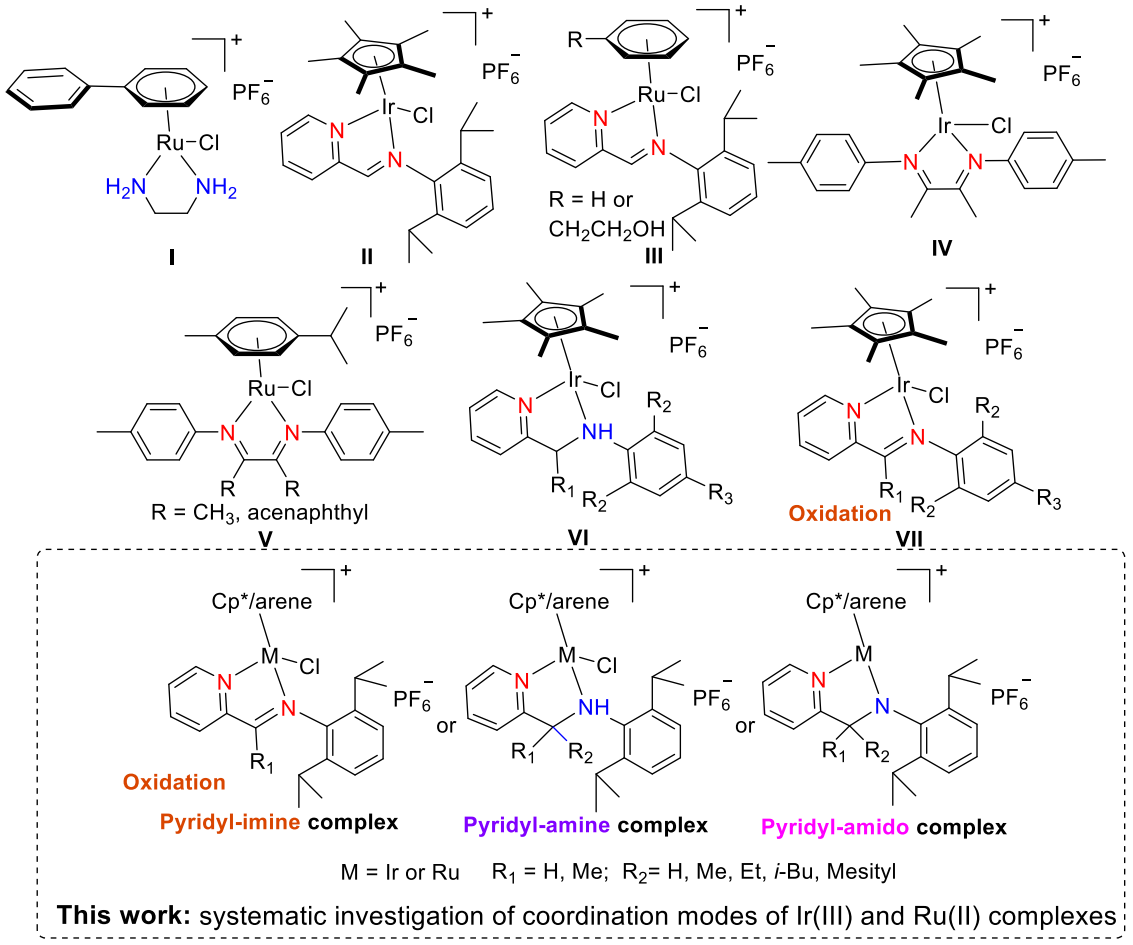

Scheme 2. Synthesis of Ligands L1−L6

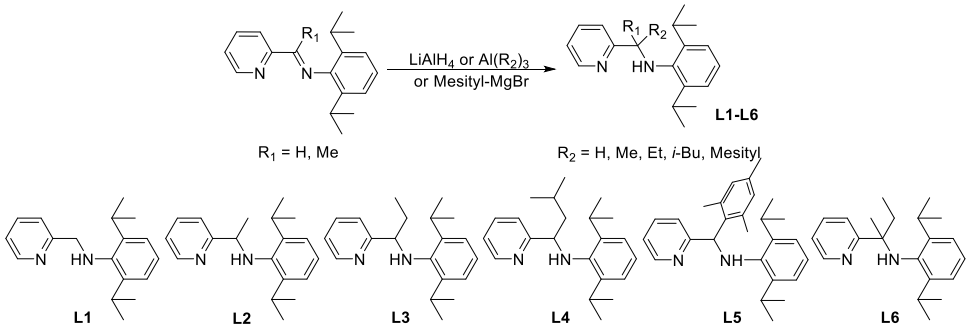

Furthermore, by varying reaction conditions (e.g., nitrogen vs adventitious oxygen atmospheres) and ligand structures, we successfully isolated three distinct types of complexes: pyridyl−amine iridium(III) complexes, their oxidized pyridyl−imine counterparts, and pyridyl−amido complexes. This preliminary observation of oxygen- and ligand-dependent structural diversity prompted us to conduct a systematic investigation of the coordination chemistry of iridium(III) complexes based on pyridyl−amine ligands. Additionally, we are intrigued by how a different metal center, such as ruthenium(II), might influence coordination behavior. Thus, our study was also extended to systematically investigate the coordination chemistry of the corresponding ruthenium(II) complexes. We found that increasing the steric bulk of substituents on the bridge carbon linking the pyridyl and amine moieties effectively suppressed oxidation. Notably, introducing a highly sterically demanding group resulted in the direct formation of a stable pyridyl−amido 16-electron complex without oxidation (Scheme 1). Moreover, the coordination chemistry of these complexes was also significantly influenced by the metal center (iridium(III) vs ruthenium(II)). In particular, the cytotoxicity and potential MoAs of these pyridyl−amine and 16-electron pyridyl−amido iridium(III) and ruthenium(II) complexes were also systematically examined in vitro.

https://doi.org/10.1021/acs.inorgchem.4c05599
Inorg. Chem. 2025, 64, 10379−10401

Scheme 3. Coordination Structures and Oxidation Tendencies of iridium(III) Complexes with Varying Steric Ligands Synthesized in This System

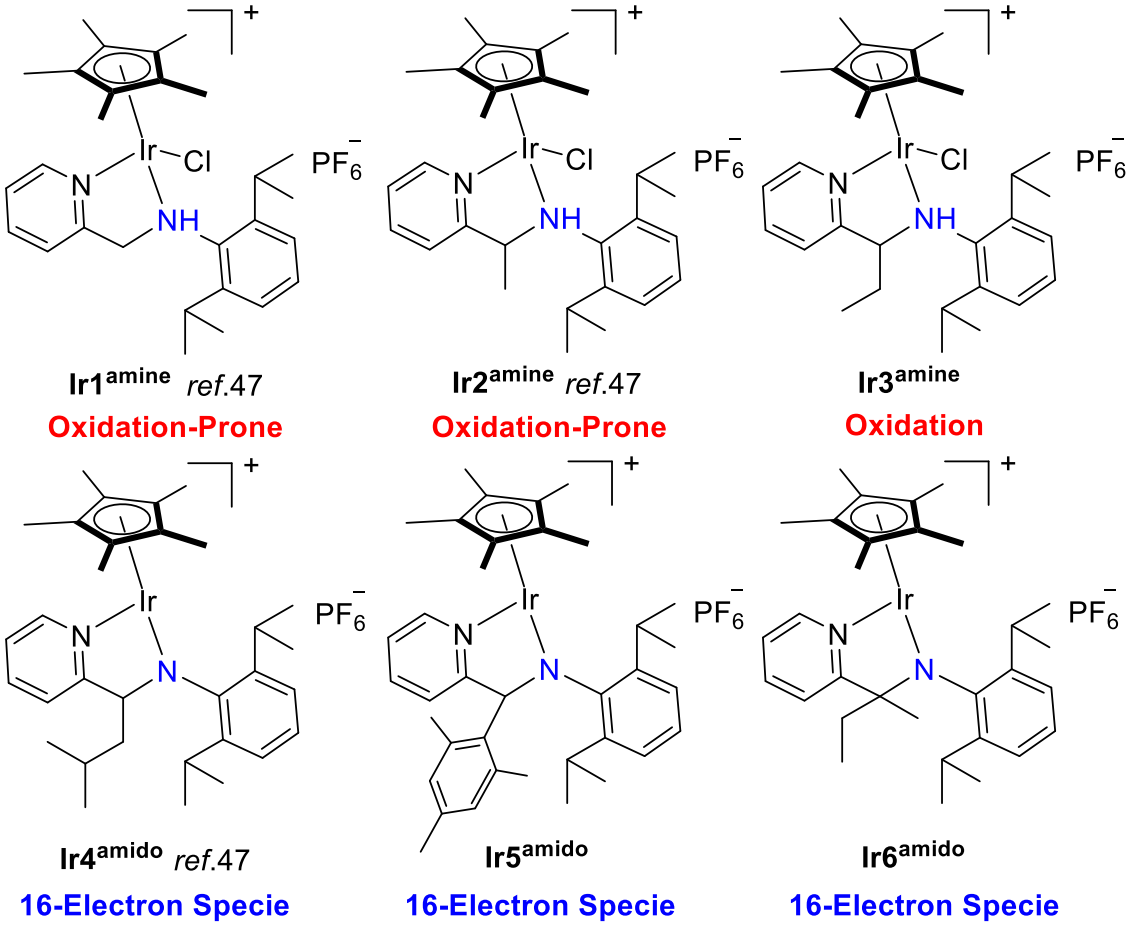

2. RESULTS AND DISCUSSION

2.1. Synthesis of Ligands. Pyridine−amine ligands **L1**−**L6** were obtained in moderate yields through the reduction of pyridine−imine compounds using different reduction agents, such as $LiAlH_4$, $AlMe_3$, $AlEt_3$, $Al(i\text{-}Bu)_3$ and 2,4,6-Me_3Ph (Mesityl)-MgBr (Scheme 2). Thus, the steric bulk of bridge carbon substituents between the pyridyl and amine groups can be adjusted using various reduction agents. Ligands **L1**, **L2**, **L4** and **L5** were previously known.[47,48] The identity and purity of new ligands **L3** and **L6** were also verified by ^{1}H NMR, ^{13}C NMR (Figures S1−S4), and mass spectrometry (Figures S26 and S27). In the ^{1}H NMR spectra, the characteristic peaks of these ligands appeared at 4.08−4.34 ppm, corresponding to the N−H proton.

2.2. Synthesis of Iridium(III) and Ruthenium(II) Complexes. Our previous study demonstrated that the reactions of pyridine−amine ligands **L1** or **L2** with $[(\eta^5\text{-}Cp^*)IrCl_2]_2$ (**D1**) ($Cp^* = C_5(CH_3)_5$) in methanol for 2 h, under trace amounts of adventitious oxygen (with no nitrogen degassing, and the oxygen present was simply that mixed into the system from the ambient air), produced a mixture of pyridyl−amine complexes (Scheme 3, **Ir1**^{amine} or **Ir2**^{amine}) and their corresponding oxidation products, namely pyridyl−imine complexes (Scheme 1, **VII**).[47] The acidic N−H proton of pyridyl−amine ligands was considered to facilitate the generation of oxidized pyridyl−imine complexes.[47,49−51] Extending the reaction time from 2 to 24 h yielded oxidized pyridyl−imine iridium(III) complexes with 64.0−71.5% yields.[47] These results indicate that both **Ir1**^{amine} and **Ir2**^{amine} undergo oxidation within a short reaction time, highlighting their susceptibility to oxidation (oxidation-prone, Scheme 3). Most interestingly, replacing H or CH_3 with a bulky *i*-Bu group on the bridge carbon inhibited oxidation, yielding a pyridyl−amido 16-electron complex (Scheme 3, **Ir4**^{amido}) with a clean isolated yield.[47] The formation of **Ir4**^{amido} likely occurred in situ via deprotonation of the pyridyl−amine complex and was stabilized by the steric hindrance provided by the bulky *i*-Bu group. These initial results suggest that the steric hindrance from substituents on the bridge carbon greatly impacts the coordination mode of iridium(III) complexes derived from pyridyl−amine ligands. This observation motivated us to systematically investigate these effects. To illustrate the impact of steric hindrance more comprehensively, we depicted the structures of **Ir1**^{amine}, **Ir2**^{amine} and **Ir4**^{amido} from our previous work,[47] alongside the newly synthesized complexes **Ir3**^{amine}, **Ir5**^{amido}, and **Ir6**^{amido} in this study (Scheme 3).

Under the same reaction conditions (methanol, 24 h, adventitious oxygen), the ethyl-substituted ligand (moderate steric hindrance) afforded the pyridyl−amine complex **Ir3**^{amine} (Scheme 4a and Figures S5, S6 and S28) in a 62.8% isolated yield with no immediate oxidation. However, prolonged storage (14 days in solution) resulted in gradual oxidation to form **Ir3**^{imine} (Scheme 4a), indicating that the ethyl group partially retards, but does not completely prevent oxidation. Building on our earlier observation that introducing a sterically

https://doi.org/10.1021/acs.inorgchem.4c05599
Inorg. Chem. 2025, 64, 10379−10401

Scheme 4. Synthesis of Pyridyl−Amine Complex Ir3^{amine}, Pyridyl−Imine Complex Ir3^{imine} and Pyridyl−Amido Complexes Ir5^{amido}, Ir6^{amido} and Ir7^{amido}

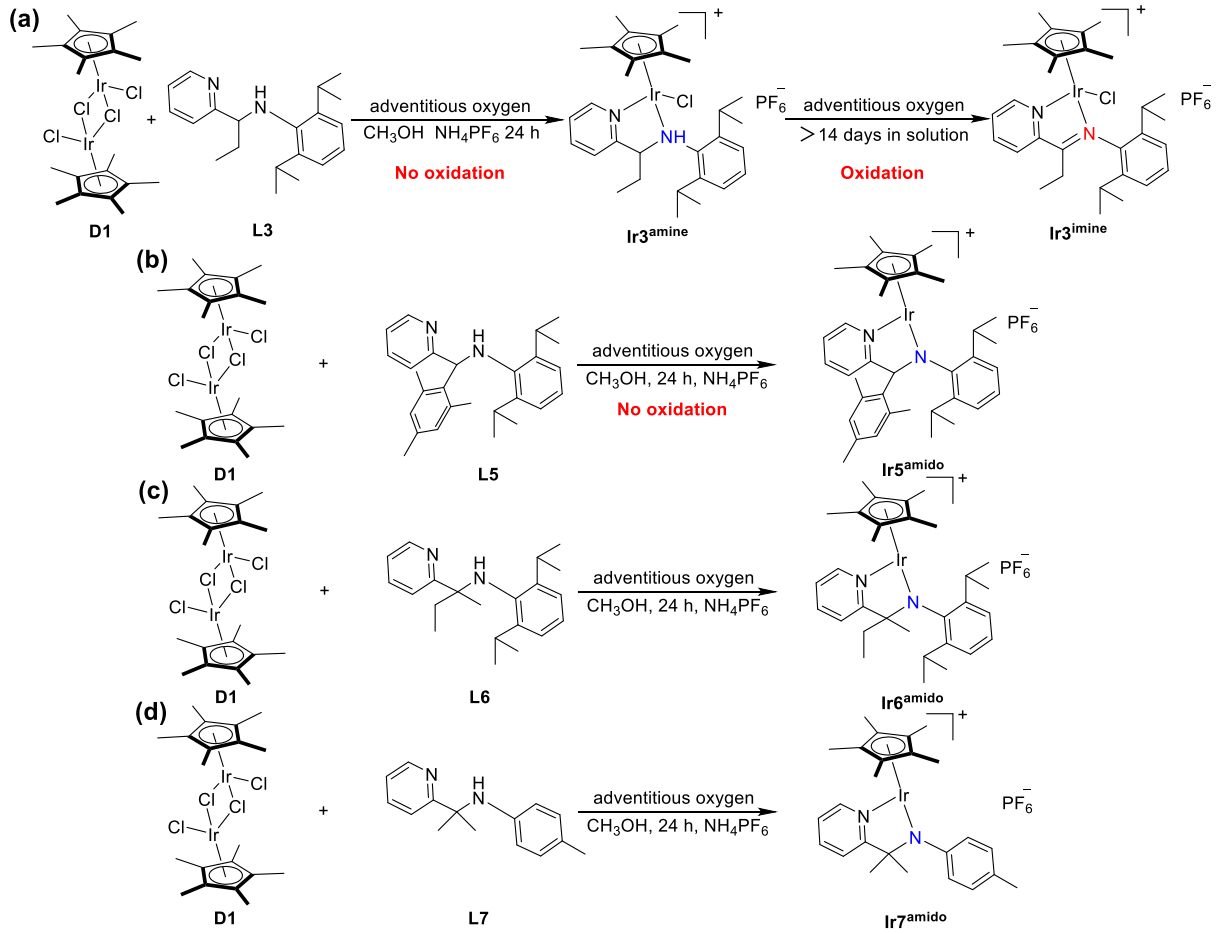

bulky *i*-Bu group prevented oxidation and led to a stable 16-electron complex (**Ir4^{amido}**),[47] we further employed a mesityl-substituted ligand with even greater steric hindrance. This approach resulted in the exclusive formation of a 16-electron pyridyl−amido complex (**Ir5^{amido}**) in 58.5% yield, with no oxidation observed (Scheme 4b). It is important to note that the presence of a *β*-hydrogen (i.e., the hydrogen attached to the bridge carbon adjacent to the metal center) in ligands **L1**−**L5** is a prerequisite for oxidation to occur. To address this issue, we synthesized ligand **L6** (Scheme 2), which features a quaternary carbon on the bridge substituted with Me and Et groups, thereby lacking any *β*-hydrogen. Reaction of **L6** with **D1** yielded a stable 16-electron pyridyl−amido complex **Ir6^{amido}**, rather than the pyridyl−amine complex (Scheme 4c). These observations demonstrate that the simultaneous introduction of bulky substituents on the bridge carbon, such as Me and Et in **Ir6^{amido}** significantly enhances steric hindrance, which effectively prevents oxidation and results in the generation of stable 16-electron pyridyl−amido complexes. To confirm the 16-electron structure of **Ir6^{amido}**, we used a similar ligand **L7**, which also features a quaternary carbon on the bridge with two methyl substituents. Reacting **L7** with **D1** yielded **Ir7^{amido}** (Scheme 4d), and single crystals were successfully obtained. The 16-electron structure of **Ir7^{amido}** was confirmed through single-crystal analysis (see Section 2.4: X-ray Crystallography). These observations emphasized the crucial influence of steric effects on stabilizing complexes and modulating their oxidation behavior.

We were also interested in systematically investigating the coordination modes of pyridyl−amine-based complexes when the metal center was switched to ruthenium(II) (Scheme 5). The reaction of ligand **L1** with the dimer $[(\eta^6\text{-}p\text{-cymene})\text{-}RuCl_2]_2$ (**D2**) in methanol for 2 h produced the pyridyl−amine complex **Ru1^{amine}** in a 61.7% yield (Scheme 6a, Figures S14, S15 and S33). Additionally, extending the reaction time from 2 to 24 h yielded a mixture of pyridyl−amine and the corresponding oxidized pyridyl−imine complex (Scheme 6b), with a molar ratio of 3:1 as determined using ^{1}H NMR spectroscopy (Figure S39). When the reaction time was further extended to 96 h, only the oxidized pyridyl−imine complex was obtained (Scheme 6c and Figure S39). These results indicates that prolonged reaction time promotes oxidation of **Ru1^{amine}** under conditions of adventitious oxygen.

When using the methyl-substituted ligand **L2**, reactions conducted for 2 or 24 h produced only pyridyl−amine complexes (yielding **Ru2^{amine}** at 61.4%, Scheme 7a and Figure S40). However, extending the reaction time to 96 h resulted in a 1:1 mixture of pyridyl−amine and pyridyl−imine complexes (Scheme 7b and Figure S40).

Compared to the unsubstituted ligand **L1**, the methyl substituent increases steric hindrance, making the complex more resistant to oxidation. Moreover, for both **L1** and **L2**, using dichloromethane instead of methanol—even up to 96

https://doi.org/10.1021/acs.inorgchem.4c05599
Inorg. Chem. 2025, 64, 10379−10401

Scheme 5. Coordination Structures and Oxidation Tendencies of ruthenium(II) Complexes with Varying Steric Ligands Synthesized in This System

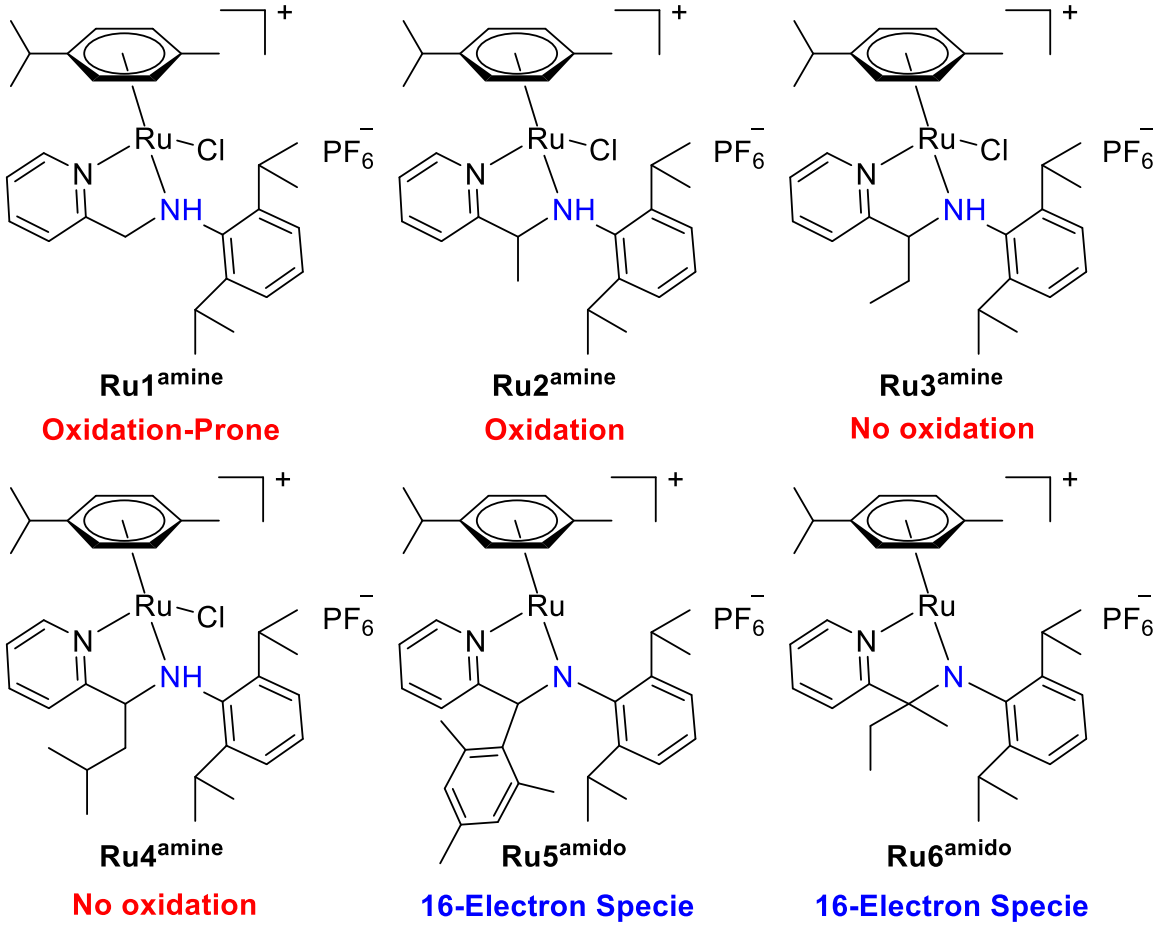

Scheme 6. Results of the Reaction between D2 and L1 in the Presence of Small Amounts of Adventitious Molecular Oxygen under the Reaction Time of (a) 2, (b) 24 or (c) 96 h in CH_3OH

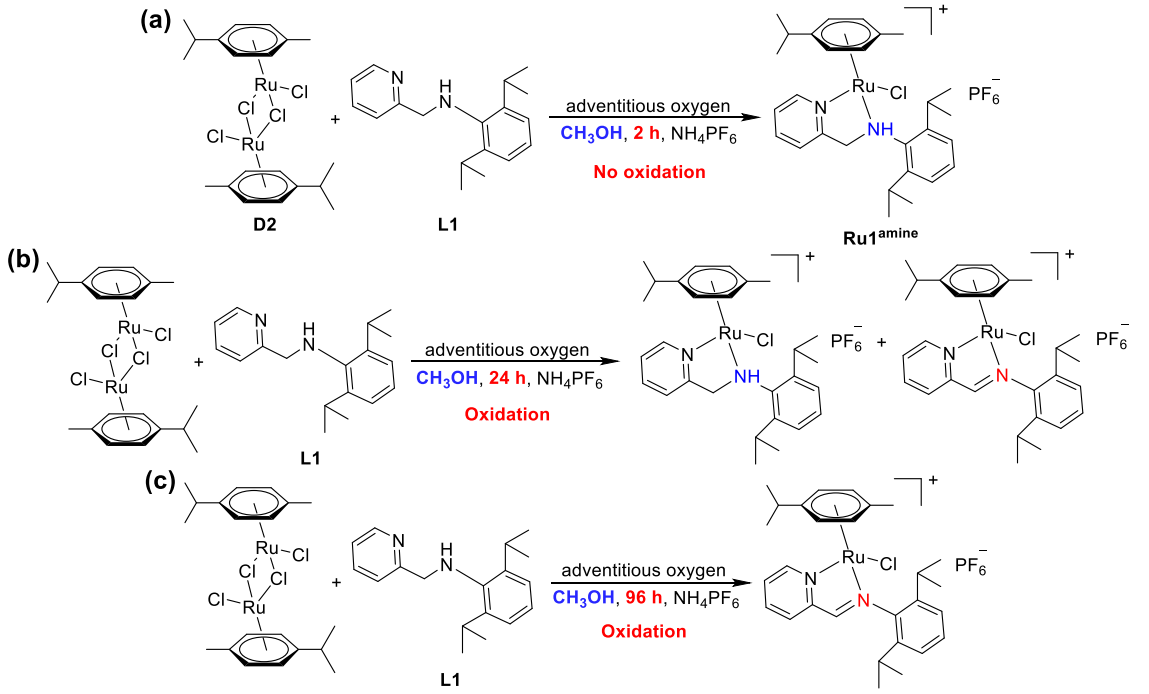

https://doi.org/10.1021/acs.inorgchem.4c05599
Inorg. Chem. 2025, 64, 10379−10401

Scheme 7. Results of the Reaction between D2 and L2 in the Presence of Small Amounts of Adventitious Molecular Oxygen under the Reaction Time of (a) 2, 24 or (b) 96 h in CH_3OH and Synthesis of Pyridyl−Amine Complexes $Ru1^{amine}$ and $Ru2^{amine}$ in the Presence of Small Amounts of Adventitious Molecular Oxygen under the Reaction Time of 2, 24, or 96 h in the Non-Polar Solvent CH_2Cl_2 (c)

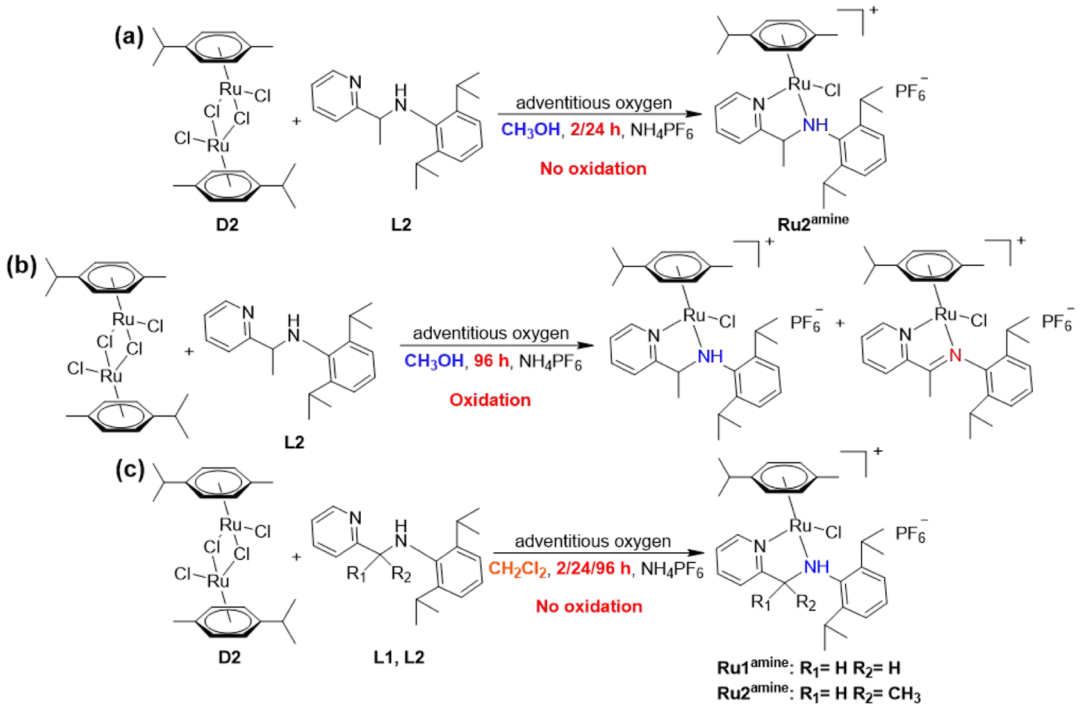

h—results exclusively in pyridyl−amine complexes (Scheme 7c, Figures S41 and S42). This is likely because the nonpolar dichloromethane inhibits deprotonation, reducing the N−H acidity and thereby preventing oxidation.

Using the bulky ethyl-substituted ligand **L3**, no oxidation was observed in either methanol or dichloromethane, even after 96 h (Scheme 8a, Figures S43 and S44). The pyridyl−amine complex $\mathbf{Ru3}^{amine}$ was isolated in a 61.1% yield after 24 h in methanol. Similarly, increasing the steric hindrance further to the *i*-Bu group (**L4**) also prevented oxidation. However, unlike the *i*-Bu-substituted iridium(III) complex $\mathbf{Ir4}^{amido}$ (which forms a 16-electron structure), the product $\mathbf{Ru4}^{amine}$ remained a highly oxidation-resistant pyridyl−amine complex (Scheme 8b), showing no oxidation even after 14 days in methanol, and was isolated in a 68.6% yield. When the mesityl-substituted ligand **L5** (with exceptionally high steric hindrance) was reacted with **D2**, a 16-electron pyridyl−amido complex $\mathbf{Ru5}^{amido}$ was formed (Scheme 8c). Likewise, using ligand **L6**—which features a quaternary bridge carbon (substituted with Me and Et) and lacks a *β*-hydrogen—yielded a 16-electron pyridyl−amido complex $\mathbf{Ru6}^{amido}$ (Scheme 8d), consistent with the behavior observed in the iridium(III) system. Additionally, we conducted a comparison experiment in which molecular oxygen was deliberately introduced into the reaction system by bubbling oxygen through the reaction mixture to increase the oxygen concentration and fully saturate the system, while maintaining the same reaction conditions. Specifically, for $\mathbf{Ru3}^{amine}$ and $\mathbf{Ru4}^{amine}$, despite the introduction of a higher oxygen concentration, no oxidation occurred, and the reaction products remained exclusively pyridyl−amine complexes (Figure S45), similar to those obtained under trace oxygen conditions. This indicates that increasing the oxygen concentration did not alter the reaction outcome.

2.3. Characterization and Reactivity of Iridium(III) and Ruthenium(II) Complexes. Comprehensive spectroscopic and analytical methods including ^1H and ^{13}C NMR spectroscopy (Figures S5−S25), mass spectrometry (Figures S28−S38), and elemental analysis have been employed to characterize all of these new complexes. For example, ^1H NMR spectroscopy of $\mathbf{Ir3}^{amine}$ revealed two distinct signals corresponding to the N−H proton at 7.12 ppm and the CH−N proton at 5.36 ppm (Figure S5), confirming the amine-metal coordination via an sp^3-N donor. The ^1H NMR spectra of representative ruthenium complex $\mathbf{Ru1}^{amine}$ also displayed two distinct peaks: one for the N−H proton at 6.80 ppm and another for the CH_2−N protons at 4.40 and 4.59 ppm (Figure S14). In the case of $\mathbf{Ru1}^{amine}$, the CH_2 group signals appeared separately, attributed to the two diastereomeric protons, consistent with previously reported pyridyl−amine iridium(II) complexes.[47] The solution stability of $\mathbf{Ir3}^{amine}$ and $\mathbf{Ru3}^{amine}$ was verified using ^1H NMR spectroscopy, with no changes observed over a period of 96 h (Figures S46 and S47), demonstrating its good stability.

^1H and ^{13}C NMR spectra for the 16-electron pyridyl−amido complexes ($\mathbf{Ir5}^{amido}$, $\mathbf{Ir6}^{amido}$, $\mathbf{Ru5}^{amido}$ and $\mathbf{Ru6}^{amido}$) displayed high stability over extended periods (e.g., 24 h in $CDCl_3$). Previous studies revealed that 16-electron half-sandwich iridium(III) complexes interact with various two-electron donors to yield stable 18-electron complexes.[52,53] However, adding PPh_3, CH_3CN, or CO to an NMR solution of $\mathbf{Ir5}^{amido}$ and $\mathbf{Ru5}^{amido}$ in $CDCl_3$ (for CH_3CN and CO) or DMSO-d_6 (for PPh_3) showed no changes in ^1H NMR peaks after 24 h (Figures S48−S53). This indicates that $\mathbf{Ir5}^{amido}$ and $\mathbf{Ru5}^{amido}$ remained unreactive toward these two-electron donors under the tested conditions. These results further confirm the exceptional stability of 16-electron pyridyl−amido iridium(III)

https://doi.org/10.1021/acs.inorgchem.4c05599
Inorg. Chem. 2025, 64, 10379−10401

Scheme 8. Synthesis of Pyridyl−Amine Complex Ru3^{amine}, Ru4^{amine}, Pyridyl−Amido Complexes Ru5^{amido}, Ru6^{amido}. Synthesis of Pyridyl−Amine Complex Ru3^{amine} in the Presence of Small Amounts of Adventitious Molecular Oxygen under the Reaction Time of 2, 24, or 96 h in CH_3OH or CH_2Cl_2

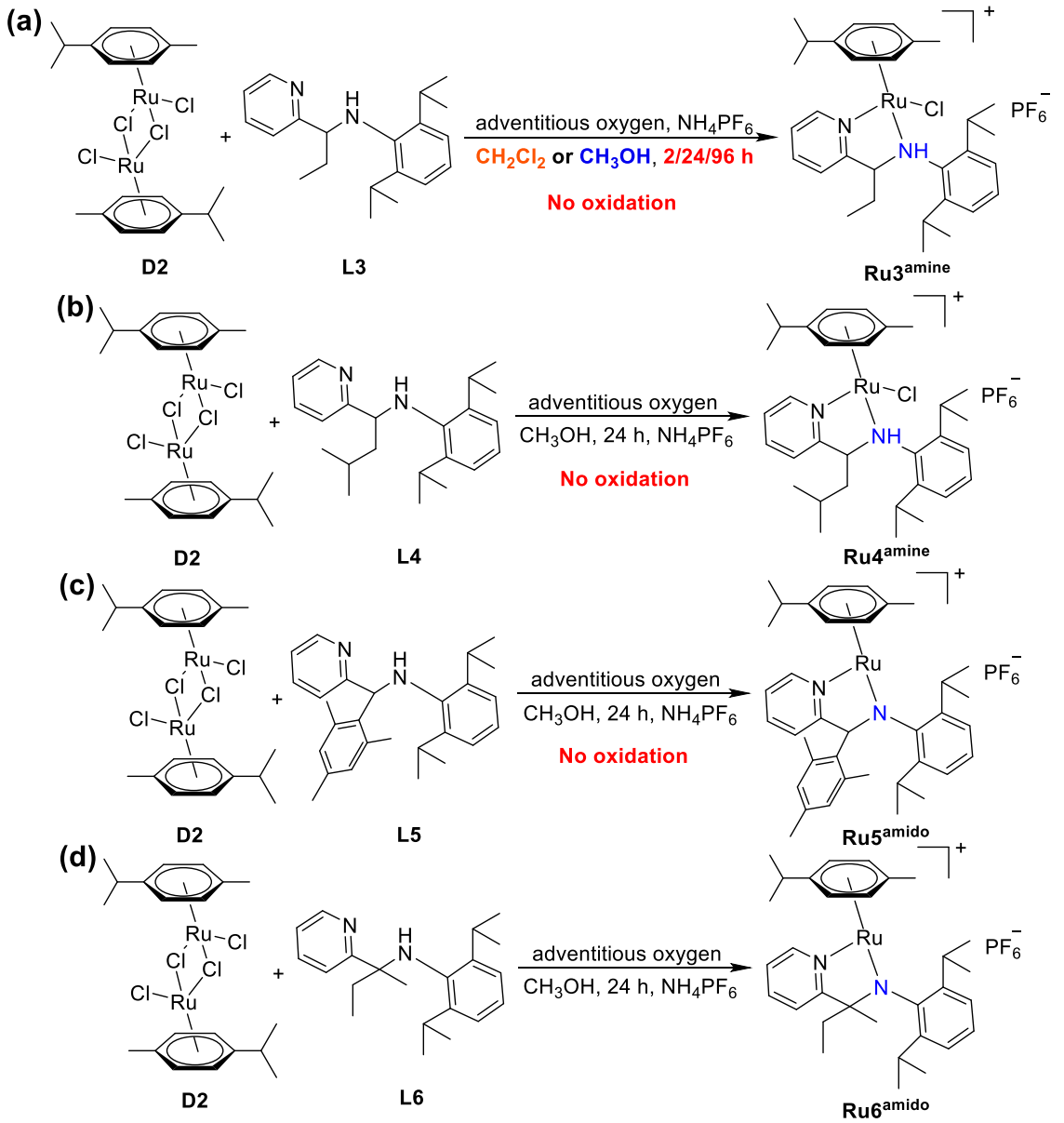

and ruthenium(II) complexes in this system. Additionally, a noticeable color difference was observed: while the 18-electron pyridyl−amine complexes (e.g., **Ir3**^{amine}, **Ru3**^{amine}) typically exhibit orange or yellow hues, the 16-electron pyridyl−amido complexes display deeper red (e.g., **Ir5**^{amido} and **Ir6**^{amido}) or deep purple (e.g., **Ru5**^{amido} and **Ru6**^{amido}) colors (Figure S54), further corroborating the differences in their coordination modes.

2.4. X-ray Crystallography. A dedicated X-ray crystallographic study was carried out to unambiguously determine the coordination geometries and structural parameters of selected complexes (Figure 1 and Table S1−S8). For the iridium(III) series, single-crystal X-ray diffraction analysis of **Ir3**^{amine} confirmed the formation of a nonplanar five-membered metallacycle involving the Ir center and the ligand's sp^3-N donor atoms. The observed C6−N2 bond length of 1.490(10) Å is characteristic of a single C−N bond, and a coordinated Cl^- ion was clearly identified at the metal center (Figure 1a and Table S1). In contrast, crystals of the oxidized product **Ir3**^{imine}, obtained after 14 days in solution, displayed a planar five-membered metallacycle. The planar structure arises from the coplanarity of the newly formed C═N double bond (C6−N2 bond length of 1.266(10) Å) and the adjacent pyridyl moiety (Figure 1b and Table S2). Additionally, **Ir5**^{amido} displayed a five-coordinated piano-stool structure, lacking a Cl^- leaving group at the metal center (16-electron). A nonplanar five-membered metallacycle was identified, with a C6−N2 bond length of 1.465(12) Å (Figure 1c and Table S3), aligning with a single C−N bond. Furthermore, although multiple attempts to crystallize the 16-electron **Ir6**^{amido} were unsuccessful, the use of a similar bridge carbon structure (also a quaternary carbon) with two methyl substituents on the ligand (**L7**), enabled the isolation and crystallographic determination of 16-electron **Ir7**^{amido} (Scheme 4d, Figure 1d

https://doi.org/10.1021/acs.inorgchem.4c05599
Inorg. Chem. 2025, 64, 10379−10401

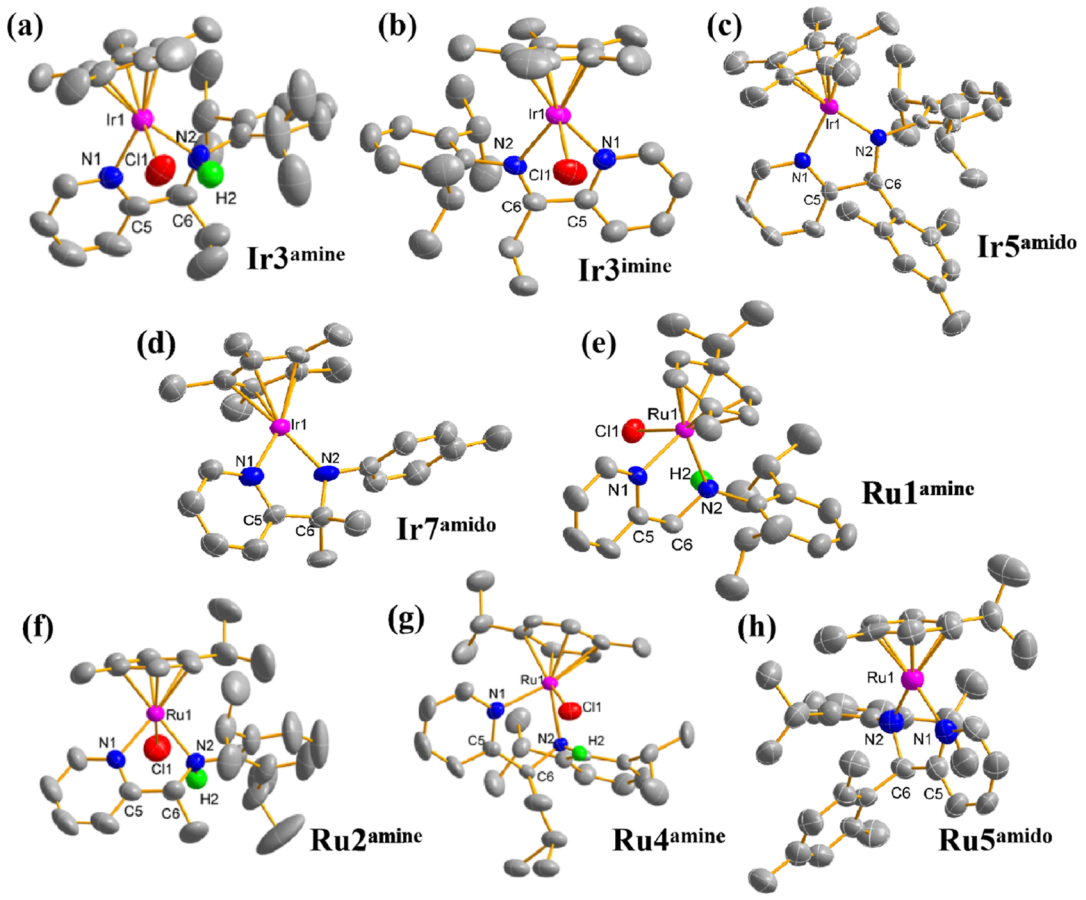

Figure 1. X-ray crystal structures of complexes **Ir3**^{amine} (a), **Ir3**^{imine} (b), **Ir5**^{amido} (c), **Ir7**^{amido} (d), **Ru1**^{amine} (e), **Ru2**^{amine} (f), **Ru4**^{amine} (g) and **Ru5**^{amido} (h) with the thermal ellipsoids drawn at the 50% probability level. The hydrogen atoms in all of these complexes and PF_6^- in **Ir3**^{amine}, **Ir3**^{imine}, **Ir5**^{amido}, **Ir7**^{amido}, **Ru1**^{amine}, **Ru2**^{amine}, **Ru4**^{amine} and **Ru5**^{amido} have been omitted for clarity.

and Table S4), also confirming the formation of a 16-electron pyridyl−amido structure of analogue **Ir6**^{amido}. For the ruthenium(II) complexes, X-ray data obtained for **Ru1**^{amine}, **Ru2**^{amine} and **Ru4**^{amine} revealed a nonplanar five-membered metallacycle with a C6−N2 bond length of 1.500(3), 1512(3) and 1.469(5) Å (Figure 1e−g and Tables S5−S7), respectively, consistent with a single C−N bond, supporting the amine-metal coordination mode. However, **Ru5**^{amido} displayed a 16-electron five-coordinated piano-stool structure, without a Cl^- leaving group at the metal center. Similarly, a nonplanar five-membered metallacycle was noted in **Ru5**^{amido} (Figure 1h and Table S8), with a C6−N2 bond length of 1.523(13) Å, indicating a single C−N bond.

2.5. Differences between Coordination Chemistry of Iridium(III) and Ruthenium(II) Complexes. Steric hindrance is crucial in influencing the oxidation behavior of both iridium(III) and ruthenium(II) complexes. Larger substituents on the bridge carbon effectively suppress oxidation and stabilize the 16-electron species. Specifically, in both iridium(III) and ruthenium(II) systems, smaller substituents like H and Me on the bridge carbon result in complexes that are more susceptible to oxidation. By contrast, introducing bulkier substituents such as Et, *i*-Bu, or mesityl significantly increases steric hindrance, which prevents oxidation and leads to the formation of stable oxidation-resistant pyridyl−amine complexes or pyridyl−amido 16-electron complexes. Iridium(III) complexes are inherently more prone to oxidation. When smaller substituents are present, oxidation occurs rapidly under standard conditions. However, the introduction of steric hindrance with substituents like *i*-Bu or mesityl leads to the generation of stable pyridyl−amido 16-electron complexes (e.g., **Ir4**^{amido}, **Ir5**^{amido}), where oxidation is effectively suppressed. In contrast, ruthenium(II) complexes exhibit higher intrinsic resistance to oxidation. Even with smaller substituents like H or Me, oxidation proceeds more slowly and requires extended reaction times or specific conditions to form oxidized products. For bulkier substituents such as Et, *i*-Bu, or mesityl, oxidation is entirely suppressed, resulting in stable pyridyl−amine (**Ru4**^{amine}), or pyridyl−amido complexes (**Ru5**^{amido}). The observed differences can be attributed to the inherent electronic properties of the two metals. Iridium, as a heavier group 9 metal, exhibits stronger π-backbonding capabilities, which stabilize low-valent or electron-deficient states like the 16-electron configuration. This greater propensity for electron deficiency makes iridium(III) complexes more susceptible to oxidation when steric protection is insufficient. Ruthenium, as a group 8 metal, has weaker π-backbonding interactions with ligands, favoring more electron-rich 18-electron configurations. This electronic preference enhances the stability of ruthenium(II) complexes against oxidation, even in cases with less steric hindrance.

2.6. Proposed Mechanism for the Oxidative Dehydrogenation of Pyridyl−Amine Complexes. Previous studies have demonstrated that the N−H proton in pyridyl−amine ligands can facilitate the oxidation of pyridyl−amine complexes to pyridyl−imine complexes upon exposure to

https://doi.org/10.1021/acs.inorgchem.4c05599
Inorg. Chem. 2025, 64, 10379−10401

adventitious oxygen.[51] Building on Gómez et al.'s reported mechanism for amine to imine oxidation,[49] the proposed oxidation mechanism of **M$^{III/II}$amine** to **M$^{III/II}$imine** in this system is illustrated in Figure 2. The production of H_2O_2

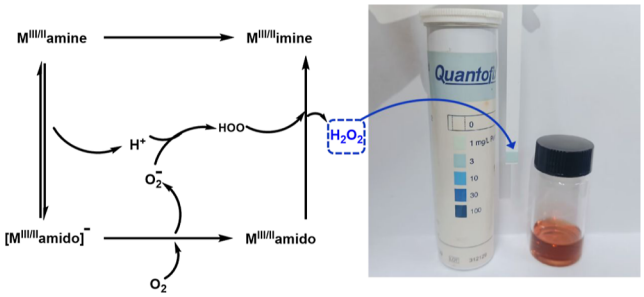

Figure 2. Proposed oxidation mechanism of pyridyl−amine to pyridyl−imine complexes, with hydrogen peroxide detected in the **Ru1^{amine}** solution after 24 h.

during the oxidation reaction in the preparation of **Ru1^{amine}** and **Ru2^{amine}** was confirmed using Quantofix peroxide test strips, which turned light blue (Scheme 6b,c, Scheme 7b, Figures 2, S55b,c, and S57c). In contrast, for reactions where no oxidation occurred, no H_2O_2 was detected using the same test strips (Figures S55a, S56, S57a,b, S58, S59 and S60). The presence of H_2O_2 was also determined by iodometry.[54] Reaction solutions collected at various time points were mixed with 2 mL of a 0.1 M acetic acid solution in methanol and 2 mL of a 0.4 M potassium iodide (KI) solution in methanol, then allowed to stand for 30 min. Under acidic conditions, H_2O_2 reacts with iodide ions (I^-) to form triiodide ions (I_3^-), which exhibit strong absorption near 355 nm. The experimental data indicated that a trace amount of hydrogen peroxide was generated during the oxidative transformation of the complex, with its concentration progressively increasing as the reaction time lengthened and the oxidation level intensified (Figure S61). The stability of 16-electron pyridyl−amido complexes, such as those formed with bulky substituents (*i*-Bu, mesityl, or disubstituted groups), further supports the proposed oxidation mechanism (Figure 2). These pyridyl−amido complexes may be generated in situ through deprotonation of the pyridyl−amine complexes and exhibit significant stability, which likely prevents further oxidation by molecular oxygen. Additionally, the nonpolar nature of dichloromethane (CH_2Cl_2) appears to hinder the deprotonation of pyridyl−amine complexes by reducing the N−H proton's acidity. This reduced acidity may suppress or completely prevent the generation of oxidized pyridyl−imine complexes.

2.7. Aqueous Stability. Evaluating the stability of metal complexes in aqueous and biological conditions is essential in drug development. It has been previously reported that half-sandwich iridium(III) and ruthenium(II) pyridyl−imine complexes are prone to hydrolysis.[41,42] Specifically, pyridyl−imine iridium(III) complexes, synthesized by reacting pyridine−imine ligands with dimer precursor $[(\eta^5\text{-Cp}^*)\text{-}MCl_2]_2$, were found to undergo M−Cl hydrolysis (Cl^-/H_2O exchange) in aqueous media.[41] Hydrolysis is often seen as an activation process, making the aqua complex (M−OH_2) more reactive than the chloride-bound (M−Cl) form in some metal-based anticancer complexes.[38,55] In our previous work, we demonstrated that **Ir1^{amine}** and **Ir2^{amine}**, when introduced into aqueous media, could undergo simultaneous oxidation and M−Cl bond hydrolysis.[47] In contrast, the 16-electron pyridyl−amido complex **Ir4^{amido}** exhibited significantly greater stability under similar conditions. UV−vis spectroscopy indicated only minor changes in its spectral profile, and ^{1}H NMR analysis confirmed that most of the parent complex remained intact.[47] The stability of the newly synthesized complexes **Ir3^{amine}**, **Ir3^{imine}**, **Ir5^{amido}**, **Ir6^{amido}**, **Ru1^{amine}**, **Ru2^{amine}**, **Ru3^{amine}**, **Ru4^{amine}**, **Ru5^{amido}** and **Ru6^{amido}** was also evaluated at 37 °C in a solution of 20% DMSO/80% PBS (v/v, obtained from H_2O, pH ≈ 7.4, high water content solution) using UV−vis

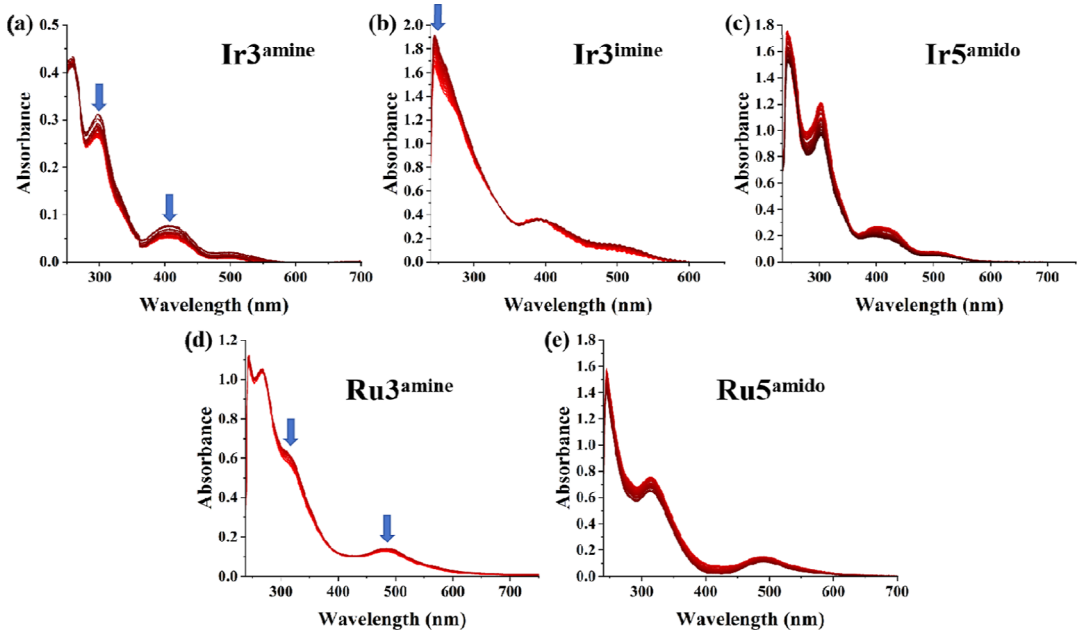

Figure 3. UV−vis spectra of **Ir3^{amine}**, **Ir3^{imine}**, **Ir5^{amido}**, **Ru3^{amine}**, and **Ru5^{amido}** over 24 h at 37 °C in 20% DMSO/80% PBS (v/v): (a) **Ir3^{amine}**; (b) **Ir3^{imine}**; (c) **Ir5^{amido}**; (d) **Ru3^{amine}**; (e) **Ru5^{amido}**.

https://doi.org/10.1021/acs.inorgchem.4c05599
Inorg. Chem. 2025, 64, 10379−10401

spectroscopy over 24 h at different time intervals (Figures 3 and S62). Changes in the absorption intensity, but without significant shifts in the absorption bands, were observed for the pyridyl−imine **Ir3**^{imine} and the pyridyl−amine **Ir3**^{amine}, **Ru1**^{amine}, **Ru2**^{amine}, **Ru3**^{amine}, and **Ru4**^{amine} (Figures 3 and S62). These results indicated that the complexes underwent hydrolysis, while the newly synthesized pyridyl−amine complexes did not undergo oxidation, likely due to their resistance to oxidation under the test conditions. By fitting the absorption changes to pseudo-first-order kinetics, we determined the half-lives ($t_1/_2$) and hydrolysis rate constants (k) for these complexes (Table 1). Overall, both the pyridyl−imine and pyridyl−amine complexes displayed relatively slow hydrolysis, with half-lives ranging from 179.6 to 231.8 min. This indicates a slower rate of hydrolysis compared to other reported half-sandwich Ir(III) and Ru(II) complexes with *N,N*-donor ligands.[56,57] Notably, the hydrolysis rates of the pyridyl−imine and pyridyl−amine complexes in this system were fairly consistent and appeared to be largely independent of the metal center or modifications to the ligands. Moreover, we also evaluated the complexes' stability under acidic conditions that mimic the cancer cell microenvironment. A solution of 20% DMSO/80% PBS (v/v) was buffered to pH 5.5 using acetic acid and sodium acetate, and stability tests were also performed at 37 °C. The results revealed that the acidic environment did not notably alter the hydrolysis rates of the complexes (Table 1 and Figure S63). Additionally, rate constants and half-lives were measured at two additional temperatures (25 and 31 °C, pH ≈ 7.4, Table 2, Figures S65 and S66). By fitting the rate constants obtained at these three temperatures (25 °C, 31 and 37 °C) to the Arrhenius equation, we calculated the activation energies (E_a, kJ/mol) for the hydrolysis of each complex (Table 2): **Ir3**^{amine} (45.87 kJ/mol), **Ir3**^{imine} (48.98 kJ/mol), **Ru1**^{amine} (51.63 kJ/mol), **Ru2**^{amine} (44.59 kJ/mol), **Ru3**^{amine} (36.21 kJ/mol) and **Ru4**^{amine} (41.68 kJ/mol). However, there is no consistent trend in activation energies as influenced by either the metal center or the ligand modifications.

Table 1. Half-Life and Hydrolysis Rate of Ir3^{amine}, Ir3^{imine}, Ru1^{amine}, Ru2^{amine}, Ru3^{amine} and Ru4^{amine} at Varying pH Levels

	20% DMSO/80% PBS pH ≈ 7.4		20% DMSO/80% PBS pH ≈ 5.5	
complexes	$t_{1/2}$ (min)	k (min^{-1})	$t_{1/2}$ (min)	k (min^{-1})
Ir3^{amine}	222.86	0.00311	235.32	0.00294
Ir3^{imine}	203.82	0.00340	220.46	0.00314
Ru1^{amine}	179.56	0.00386	199.79	0.00346
Ru2^{amine}	211.35	0.00328	248.16	0.00279
Ru3^{amine}	231.82	0.00299	252.96	0.00274
Ru4^{amine}	225.04	0.00308	238.58	0.00290

Table 2. Hydrolysis Data for Ir3^{amine}, Ir3^{imine}, Ru1^{amine}, Ru2^{amine}, Ru3^{amine} and Ru4^{amine} at Various Temperatures

	k (min^{-1}) $t_{1/2}$(min)			
complexes	25 °C	31 °C	37 °C	E_a (kJ/mol)
Ir3^{amine}	0.00235	0.00286	0.00311	45.87
	294.89	242.31	222.86	
Ir3^{imine}	0.00257	0.00305	0.00340	48.98
	269.65	227.21	203.82	
Ru1^{amine}	0.00295	0.00323	0.00386	51.63
	234.92	214.44	179.56	
Ru2^{amine}	0.00264	0.00275	0.00328	44.59
	262.50	252.00	211.35	
Ru3^{amine}	0.00242	0.00271	0.00299	36.21
	286.36	255.70	231.82	
Ru4^{amine}	0.00238	0.00286	0.00308	41.68
	291.18	242.31	225.04	

As discussed earlier, the 16-electron pyridyl−amido complexes demonstrated stability in $CDCl_3$ solution and remained unreactive with two-electron donors like CH_3CN, PPh_3 and CO. However, minor changes in the UV−vis absorption intensity of **Ir5**^{amido}, **Ir6**^{amido}, **Ru5**^{amido}, and **Ru6**^{amido} were observed after 24 h in a high-water-content solution (20% DMSO/80% PBS, v/v, obtained from H_2O, pH ≈ 7.4) at 37 °C (Figures 3c,e and S62a,e). These changes suggest that H_2O likely coordinates to the 16-electron parent complexes, leading to the partial formation of 18-electron aquated species (e.g., Ir−OH_2) in aqueous media. Under pH 5.5 conditions (20% DMSO/80% PBS, v/v, buffered to pH 5.5 with acetic acid/sodium acetate), similar changes were also observed compared to those at pH 7.4 (Figure S64). To ensure sufficient complex concentration for reliable spectroscopic measurements, the stability of **Ir3**^{amine}, **Ir3**^{imine}, **Ir5**^{amido}, **Ir6**^{amido}, **Ru1**^{amine}, **Ru2**^{amine}, **Ru3**^{amine}, **Ru4**^{amine}, **Ru5**^{amido} and **Ru6**^{amido} was also evaluated under conditions with a higher proportion of DMSO-d_6 and lower proportion of water (80% DMSO-d_6/20% PBS, v/v, obtained from D_2O, pH ≈ 7.4) at 37 °C. ^{1}H NMR spectroscopy was used to monitor the complexes over a 24 h period. For **Ir3**^{amine}, **Ru1**^{amine}, **Ru3**^{amine}, and **Ru4**^{amine}, a new set of peaks corresponding to the aqua complex was observed (Figures S67, S71 S73 and S74), indicating the hydrolysis of the Mt−Cl bond, However, the extent of hydrolysis remained low (**Ir3**^{amine}: 13%, **Ru1**^{amine}: 16%, **Ru3**^{amine}: 17%, **Ru4**^{amine}: 21%) within 24 h. In contrast, the other complexes exhibited spectra with no new peaks, and all proton assignments were consistent with their known molecular structures (Figures S69, S70, S73 and S75−S76). This indicates that no decomposition or ligand dissociation occurred during the test, confirming the stability of these complexes under reduced water content conditions. Overall, the potential of these complexes for further anticancer activity studies in aqueous conditions has been established.

2.8. Cytotoxicity. The cytotoxicity of the newly synthesized complexes, using cisplatin as a standard control, was evaluated against lung cancer A549 cells, cervical carcinoma HeLa cells, cisplatin-resistant A549/DDP cells, and non-cancerous BEAS-2B cells using the MTT assay (Table 3). Metal precursors **D1**, **D2**, and ligands **L1**-**L6** showed no cytotoxicity against these cells (IC_{50} > 100 μM). However, **Ir3**^{amine}, **Ir3**^{imine}, **Ir5**^{amido}, **Ir6**^{amido}, **Ru3**^{amine}, **Ru4**^{amine}, **Ru5**^{amido} and **Ru6**^{amido} exhibited potent cytotoxic effects against A549 and HeLa cells, with IC_{50} values ranging from 17.28 to 27.54 μM and 15.24 to 29.25 μM, respectively, which are on par with or even surpass commercial cisplatin. This suggests that the anticancer activity of these complexes is primarily due to the interaction between the free ligands and the iridium(III) or ruthenium(II) ions. It should be noted that **Ru1**^{amine} showed no activity against all three cancer cell lines, while **Ru2**^{amine} exhibited activity only against HeLa cells. However, no clear structure−activity relationship was observed between the steric bulk of the ligand substituents and the anticancer activity.

https://doi.org/10.1021/acs.inorgchem.4c05599
Inorg. Chem. 2025, 64, 10379−10401

Table 3. Cytotoxicity of the Ligands, Precursors and Complexes in Cancer and Normal Cell Lines after 48 h of Incubation

	IC_{50} (μM)				
compounds	A549	HeLa	A549/DDP	BEAS-2B	SI[a]
L1	>100	>100	>100	>100	
L2	>100	>100	>100	>100	
L3	>100	>100	>100	>100	
L4	>100	>100	>100	>100	
L5	>100	>100	>100	>100	
L6	>100	>100	>100	>100	
D1	>100	>100	>100	>100	
D2	>100	>100	>100	>100	
Ir3^{amine}	27.54 ± 0.24	22.65 ± 0.27	65.47 ± 0.12	50.28 ± 0.13	2.38
Ir3^{imine}	25.44 ± 0.26	29.25 ± 0.17	71.27 ± 0.34	63.41 ± 0.34	2.80
Ir5^{amido}	18.75 ± 0.18	19.95 ± 0.21	23.58 ± 0.30	27.39 ± 0.34	1.26
Ir6^{amido}	20.12 ± 0.57	21.25 ± 0.41	26.27 ± 0.34	29.41 ± 0.64	1.31
Ru1^{amine}	>100	>100	>100	>100	
Ru2^{amine}	>100	70.32 ± 0.25	>100	>100	
Ru3^{amine}	21.02 ± 0.21	28.24 ± 0.09	60.45 ± 0.24	41.75 ± 0.22	2.87
Ru4^{amine}	23.12 ± 0.14	29.21 ± 0.09	63.12 ± 0.17	53.72 ± 0.19	2.73
Ru5^{amido}	19.02 ± 0.21	18.24 ± 0.19	24.63 ± 0.47	31.75 ± 0.36	1.29
Ru6^{amido}	17.28 ± 0.09	15.24 ± 0.16	22.74 ± 0.29	28.64 ± 0.15	1.31
Cisplatin	24.89 ± 0.21	8.39 ± 0.08	38.14 ± 1.01	29.21 ± 0.22	1.20

[a]SI: The selectivity index is the ratio of IC_{50} values for BEAS-2B normal cells to A549 cancer cells.

Interestingly, most of these iridium(III) and ruthenium(II) complexes exhibited significant cytotoxicity against cisplatin-resistant A549/DDP cells, with IC_{50} values ranging from 22.74 to 26.27 μM, suggesting their mechanisms of action differ from cisplatin. The 16-electron pyridyl−amido complexes **Ir5^{amido}**, **Ir6^{amido}**, **Ru5^{amido}** and **Ru6^{amido}**, exhibited significantly enhanced potency (ca. 3 times greater) against A549/DDP cells compared to pyrydyl−imine complex **Ir3^{imine}** and pyridyl−amine complexes **Ir3^{amine}**, **Ru3^{amine}** and **Ru4^{amine}** with IC_{50} values of 22.74−26.27 μM versus 60.45−71.27 μM. In addition, MTT assay was conducted on noncancerous BEAS-2B cells, but no significant selectivity (SI: 1.26−2.87) was observed between cancer and normal cells. The IC_{50} values of these complexes (27.39−63.41 μM) were similar to or lower than that of cisplatin (29.21 μM).

Notably, lung cancer is a leading cause of mortality worldwide, with high fatality rates in both developed and developing countries. Given that current treatments, such as cisplatin, have not demonstrated ideal efficacy in the treatment of lung cancer, we thus selected A549 lung cancer cells as the model for the subsequent biological studies. Moreover, four representative complexes—**Ir3^{amine}**, **Ir5^{amido}**, **Ru3^{amine}**, and **Ru5^{amido}**—were selected for further biological evaluation (see Sections 2.15 below) since this selection allowed us to systematically compare the effects of different metal centers (**Ir3^{amine}** vs **Ru3^{amine}**; **Ir5^{amido}** vs **Ru5^{amido}**) and coordination modes (16-electron vs 18-electron, **Ir3^{amine}** vs **Ir5^{amido}**; **Ru3^{amine}** vs **Ru5^{amido}**).

The total cellular accumulation of complexes **Ir3^{amine}**, **Ir5^{amido}**, **Ru1^{amine}**, **Ru3^{amine}**, and **Ru5^{amido}** was quantified in A549 cancer cells treated with each complex (5 μM) for 48 h by ICP−MS to determine if there was a correlation between cellular uptake levels of the complexes and cytotoxicity. The intracellular metal accumulation (ng/μg protein) in A549 cells was determined tobe **Ir5^{amido}** (0.598) > **Ir3^{amine}** (0.514) > **Ru5^{amido}** (0.391) > **Ru1^{amine}** (0.346) ≈ **Ru3^{amine}** (0.341), indicating that iridium(III) complexes are generally more internalized than the corresponding ruthenium(II) complexes. However, no clear correlation between cellular uptake and cytotoxicity was observed. Aside from **Ru1^{amine}**, which showed no activity, the other complexes displayed similar cytotoxicity against A549 cells. Therefore, differences in cellular accumulation do not explain the variations in cytotoxicity among these complexes.

2.9. DNA and Protein Binding Results. The potential interactions of the representative complexes **Ir3^{amine}**, **Ir5^{amido}**, **Ru3^{amine}**, **Ru5^{amido}** and adriamycin (as a positive control) with Calf Thymus DNA (CT-DNA) were examined through UV−vis absorption spectroscopy (Figure S77), considering that DNA binding often contributes to the cytotoxic activity of metal-based anticancer complexes. In these experiments, solutions containing 60 μM of each complex were mixed with increasing concentrations of CT-DNA (0−43.6 μM). This resulted in hyperchromism and a slight red shift at the absorption peak, characteristic of noncovalent electrostatic binding.[41,58] The intrinsic equilibrium binding constants (K_b) were calculated using the Benesi−Hildebrand equation and found to range from 1.19×10^4 to 2.42×10^4 M^{-1} (Figure S78: **Ir3^{amine}**: $K_b = 2.42 \times 10^4$ M^{-1}, **Ir5^{amido}**: $K_b = 2.04 \times 10^4$ M^{-1}, **Ru3^{amine}**: $K_b = 1.19 \times 10^4$ M^{-1}, **Ru5^{amido}**: $K_b = 1.24 \times 10^4$ M^{-1}). These values were notably lower than those for adriamycin (11.2×10^4 M^{-1}) and for similar half-sandwich complexes in previous studies ($K_b > 10^5$ M^{-1}),[29,59,60] suggesting relatively weak CT-DNA interactions. Furthermore, the K_b did not correlate with the cytotoxicity of these complexes, indicating that DNA binding is unlikely to be the main MoA for these half-sandwich complexes.

It is crucial to understand how anticancer agents interact with cellular proteins, as these proteins are pivotal in the transport and metabolism of drugs. Serum albumin (SA), a major blood plasma protein, is known for its ability to bind and transport metal-based complexes. Bovine serum albumin (BSA) was selected as a substitute for human serum albumin (HSA) in this study due to its similar structure and easier accessibility. The interactions between **Ir3^{amine}**, **Ir5^{amido}**, **Ru3^{amine}**, **Ru5^{amido}**, fluorescein (as a positive control) and

https://doi.org/10.1021/acs.inorgchem.4c05599
Inorg. Chem. 2025, 64, 10379−10401

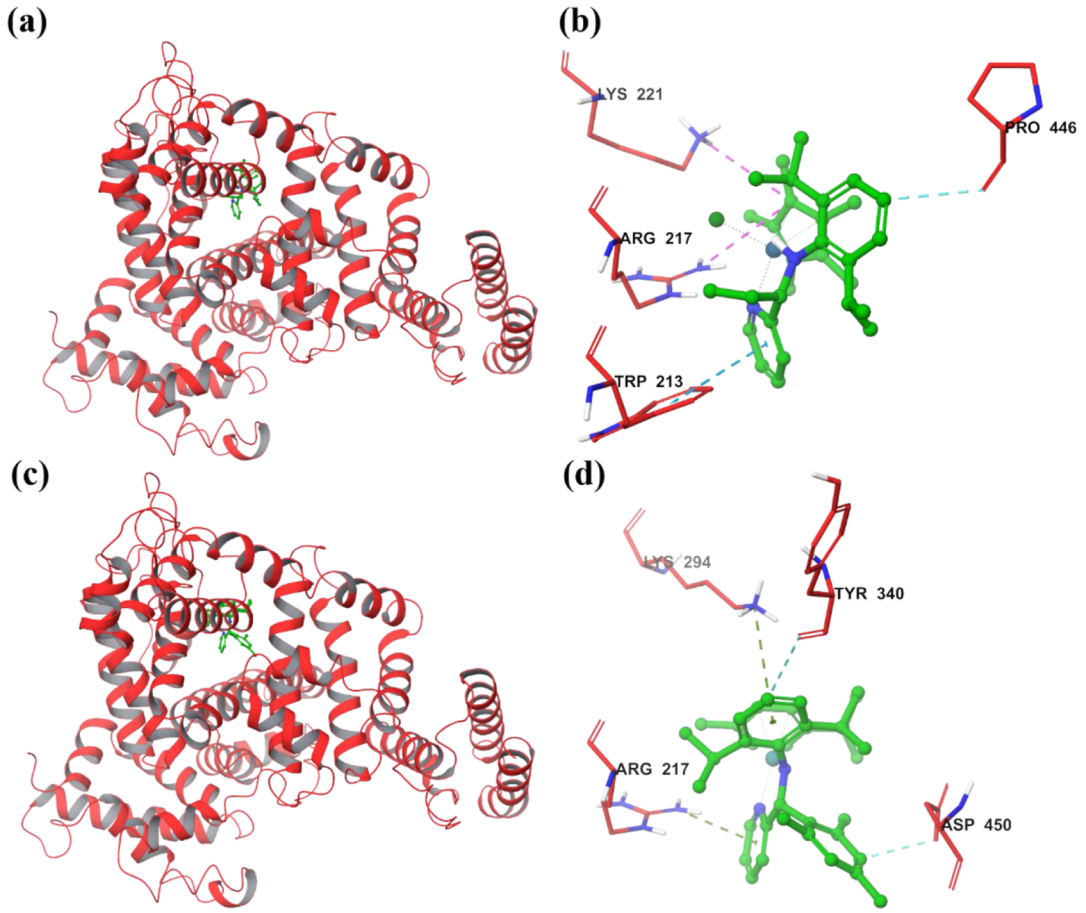

Figure 4. Docking model of complexes (a) **Ir3**^{amine} and (c) **Ru5**^{amido} positioned in the hydrophobic cavity of BSA (PDB ID: 4OR0). Interaction details between complexes (b) **Ir3**^{amine} and (d) **Ru5**^{amido} with the polypeptide chains.

BSA were investigated through UV−vis absorption and fluorescence spectroscopy (Figure S79a−e). To eliminate potential self-absorption effects, both the reference and sample cuvettes were pretreated with the respective complexes. The fluorescence behavior of BSA arises from the aromatic amino acids tyrosine (Tyr) and tryptophan (Trp), which respond to changes in their environment. Binding of small molecules to these residues can lead to a decrease in fluorescence intensity. As the complexes and fluorescein concentration increased, the absorption peak of BSA at 229 nm decreased and shifted slightly, likely due to α-helix changes and the effect of polar solvents.[61−65] Additionally, the absorption peak at 276 nm exhibited a gradual increase without a shift, indicating subtle changes in the microenvironment surrounding the aromatic residues (Tyr and Trp).[66,67] The fluorescence intensity of BSA at 353 nm steadily decreased with increasing complex or fluorescein concentration (Figure S79f−j), indicating interactions through a static quenching mechanism.[68] Synchronous fluorescence spectroscopy is an effective method for examining the conformational alterations in BSA caused by interactions with the complexes. By maintaining a fixed wavelength interval of 15 or 60 nm, this method can reveal specific alterations in the microenvironments of Tyr and Trp residues.[69,70] At $\Delta\lambda$ = 60 nm, the emission of Trp shifted to 276 nm with a 3 nm red shift. Similarly, at $\Delta\lambda$ = 15 nm, Tyr exhibited a decrease in intensity at 287 nm, accompanied by a 2 nm red shift (Figure S80), which points to changes in its microenvironment and conformation. These results imply that **Ir3**^{amine}, **Ir5**^{amido}, **Ru3**^{amine}, and **Ru5**^{amido} interact with BSA, causing subtle alterations in the structure of its aromatic residues, an effect similar to that of the positive control fluorescein.

Molecular docking studies of the selected representative 18-electron **Ir3**^{amine} and 16-electron **Ru5**^{amido} complexes were carried out using the AutoDock suite and Q-SiteFinder, which are designed to identify potential binding sites and assess ligand−protein interactions. The crystal structure of bovine serum albumin (BSA) (PDB ID: 4OR0) was retrieved from the Protein Data Bank. Initially, Q-SiteFinder was used to pinpoint probable binding regions within BSA. Docking simulations were then conducted using AutoDock, where iridium and ruthenium parameters, absent from AutoDock's default force field, were manually added to the parameter library. Flexible residues within a 6 Å radius of the binding pocket were chosen to enable adaptive docking. The docking results showed several significant interactions between **Ir3**^{amine}, **Ru5**^{amido} and BSA, including electrostatic, hydrogen bonding, and π-cation interactions (Figure 4). Specifically, the 18-electron pyridyl−amine complex **Ir3**^{amine} formed a salt bridge with LYS221 and ARG217, along with a π-cation interaction with TRP213. Additionally, a "nonconventional" hydrogen bond with PRO446 was observed. In the case of the 16-electron pyridyl−amido complex **Ru5**^{amido}, π-cation interactions were noted with LYS294 and ARG217. Several "nonconventional" hydrogen bonds were also identified, involving residues like TYR340 and ASP450. These results provide deeper insight into the binding mechanisms of **Ir3**^{amine}

https://doi.org/10.1021/acs.inorgchem.4c05599
Inorg. Chem. 2025, 64, 10379−10401

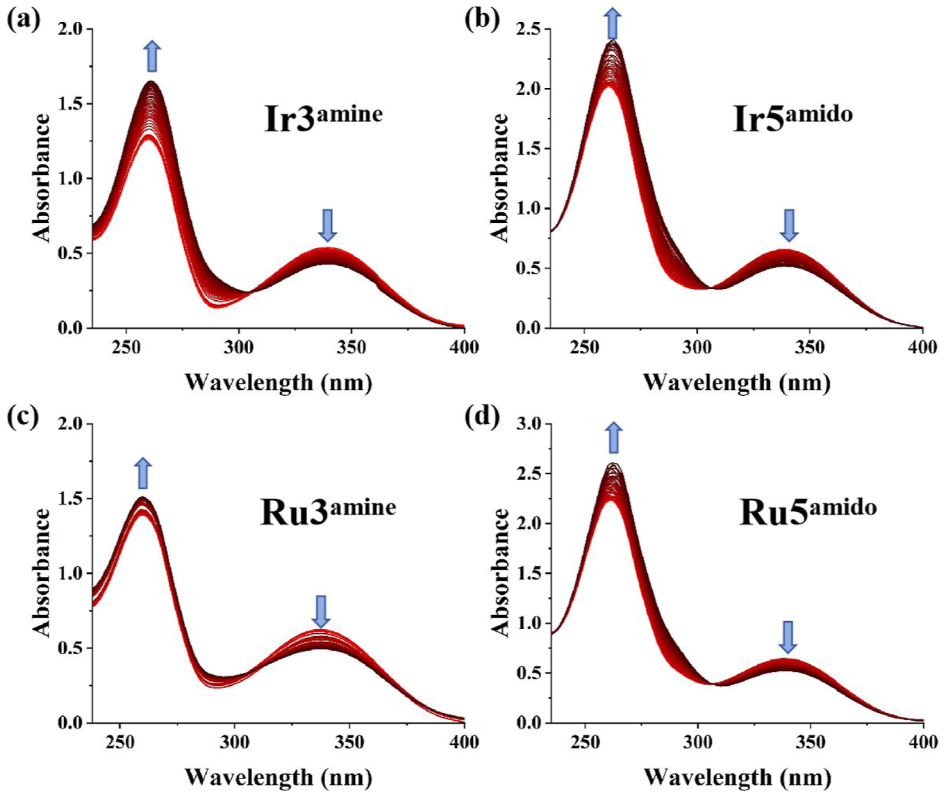

Figure 5. UV−vis spectra of the reaction between NADH (100 μM) and (a) **Ir3**^{amine}, (b) **Ir5**^{amido}, (c) **Ru3**^{amine} and (d) **Ru5**^{amido} (1 μM) in 10% MeOH/90% H_2O (v/v) at 25 °C for 8 h.

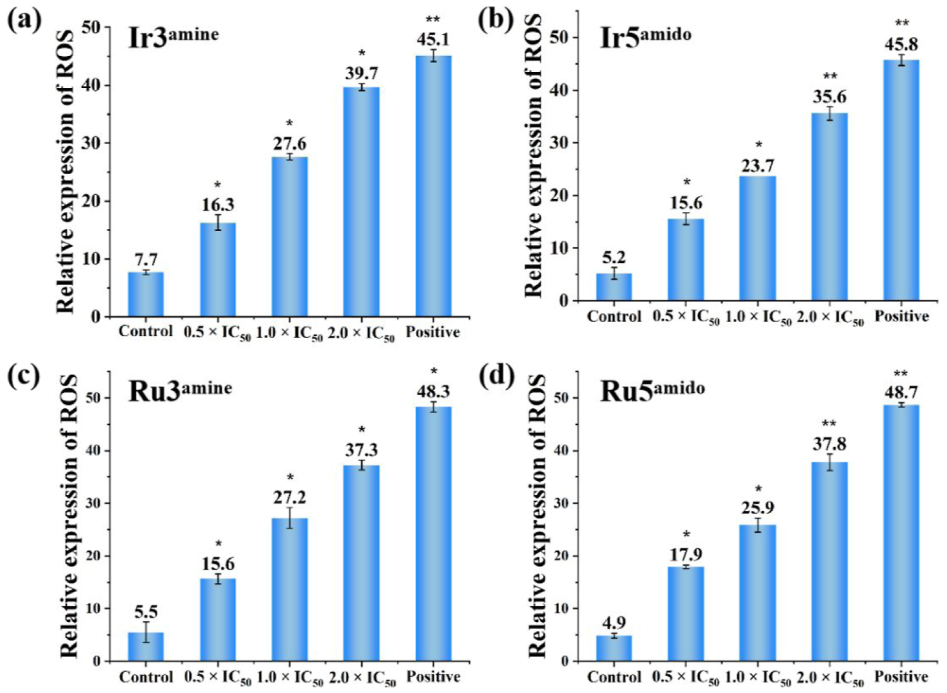

Figure 6. Fluorescence microscopy analysis of ROS levels in A549 cells after 4 h treatment with (a) **Ir3**^{amine}, (b) **Ir5**^{amido}, (c) **Ru3**^{amine}, and (d) **Ru5**^{amido} at 37 °C. Cells were stained with DCFH-DA, and ROSup served as a positive control for ROS induction. *p*-values were calculated compared to the untreated control (*p < 0.05, **p < 0.01).

and **Ru5**^{amido} with BSA, offering valuable information on their potential effects on transport, stability, and bioavailability.

2.10. Catalytic Hydride Transfer. Coenzymes nicotinamide adenine dinucleotide (NADH) and its oxidized counterpart (NAD^+) are crucial for regulating cellular balance and maintaining homeostasis. The NADH/NAD^+ ratio and NAD^+ levels are integral to various intracellular redox reactions.[71] In recent years, the use of hydride transfer catalysis in anticancer

https://doi.org/10.1021/acs.inorgchem.4c05599
Inorg. Chem. 2025, 64, 10379−10401

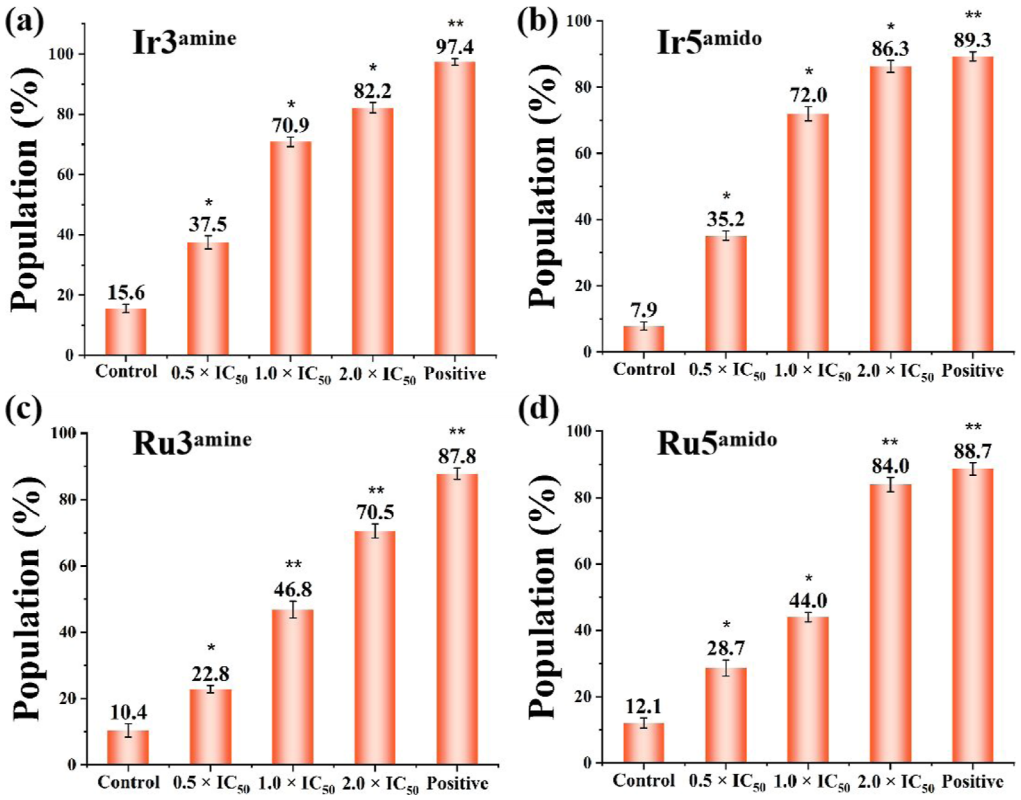

Figure 7. Changes in mitochondrial membrane potential of A549 cancer cells induced by (a) **Ir3**^{amine}, (b) **Ir5**^{amido}, (c) **Ru3**^{amine}, and (d) **Ru5**^{amido}. CCCP (Carbonyl cyanide *m*-chlorophenyl hydrazone) was used as a positive control to induce mitochondrial membrane depolarization. Data are quoted as mean ± SD of three replicates. *p*-values were calculated compared to the untreated control (*$p < 0.05$, **$p < 0.01$).

drug design has attracted considerable interest.[72] The Sadler group demonstrated that NADH can transfer a hydride to aqua iridium(III) cyclopentadienyl complexes, generating ROS such as H_2O_2, which acts as part of the oxidant MoA.[73−75] Similarly, our group revealed that half-sandwich pyridine−imine iridium(III) and ruthenium(II) complexes with sp^2-N/sp^2-N coordination can facilitate the catalytic conversion of NADH to NAD^+. This process elevates ROS levels, triggers oxidative stress, and plays a role in promoting cell death (Scheme 1, **II** and **III**).[41−43] Along this line, we also explored the catalytic hydride transfer activity of new hybrid sp^2-N/sp^3-N pyridyl−amine and pyridyl−amido complexes (**Ir3**^{amine}, **Ir5**^{amido}, **Ru3**^{amine}, and **Ru5**^{amido}) in this system. The interactions of these complexes with NADH at a molar ratio of 1:100 were monitored in a solution comprising 10% methanol and 90% water (v/v) over an 8 h period using UV−vis spectroscopy (Figure 5). A decrease in the NADH absorption peak at 339 nm was observed, indicating the occurrence of catalytic activity. Turnover numbers (TONs) were calculated as follows: 16.40 for **Ir3**^{amine}, 21.54 for **Ir5**^{amido}, 21.90 for **Ru3**^{amine}, and 18.84 for **Ru5**^{amido}. These values align with those observed for earlier pyridine−imine complexes.[41,43] To verify NADH oxidation, separate HPLC and ESI-MS experiments were also conducted (Figures S81, 82). HPLC analysis of NADH and NAD^+ standards produced distinct retention times. After incubating NADH with complex **Ir3**^{amine} at 25 °C for 24 h, the HPLC profile showed a diminished NADH peak and an emerging NAD^+ peak, indicating that **Ir3**^{amine} catalyzed the oxidation of NADH to NAD^+. Analysis of the reaction mixture by ESI-MS also revealed a NAD^+ signal at m/z 664.1 ($[M + H]^+$, Figure S82), further corroborating the oxidation of NADH. The capacity of these complexes to disrupt the NADH/NAD^+ balance may trigger ROS production and activate an oxidative mechanism, prompting further exploration of their potential ROS generation in cancer cells.

2.11. Cellular ROS Determination. Pyridyl−imine iridium(III) and ruthenium(II) complexes were found to significantly elevate ROS levels in A549 cells.[41−43,76] This prompted us to explore the impact of switching the coordination mode from pyridyl−imine to pyridyl−amine or pyridyl−amido complexes on ROS generation. ROS levels induced by the representative complexes **Ir3**^{amine}, **Ir5**^{amido}, **Ru3**^{amine} and **Ru5**^{amido} at the concentrations of 0.5, 1.0, and 2.0 × IC_{50} were determined using DCFH-DA staining and fluorescence microscopy (Figures 6 and S83). A549 cells treated with these complexes exhibited a noticeable, concentration-dependent increase in fluorescence intensity, indicating higher ROS levels compared to control cells (Figures 6a−d and S83). Thus, these complexes could potentially disturb the intracellular redox balance by generating ROS. Previous studies have shown that many half-sandwich complexes with different chelating ligands can generate ROS through catalytic hydride transfer from NADH to O_2.[77−79] Similarly, in this system, the conversion of NADH to NAD^+, as noted in Section 2.10, was also observed for these complexes, may contribute to ROS generation. Overall, these results indicate that the anticancer effects of these complexes can be attributed to the elevated ROS levels.

2.12. Mitochondrial Membrane Depolarization. Given that these complexes can induce excessive reactive oxygen species (ROS) and mitochondria are vital regulators of ROS production, we investigated whether they affect mitochondrial

https://doi.org/10.1021/acs.inorgchem.4c05599
Inorg. Chem. 2025, 64, 10379−10401

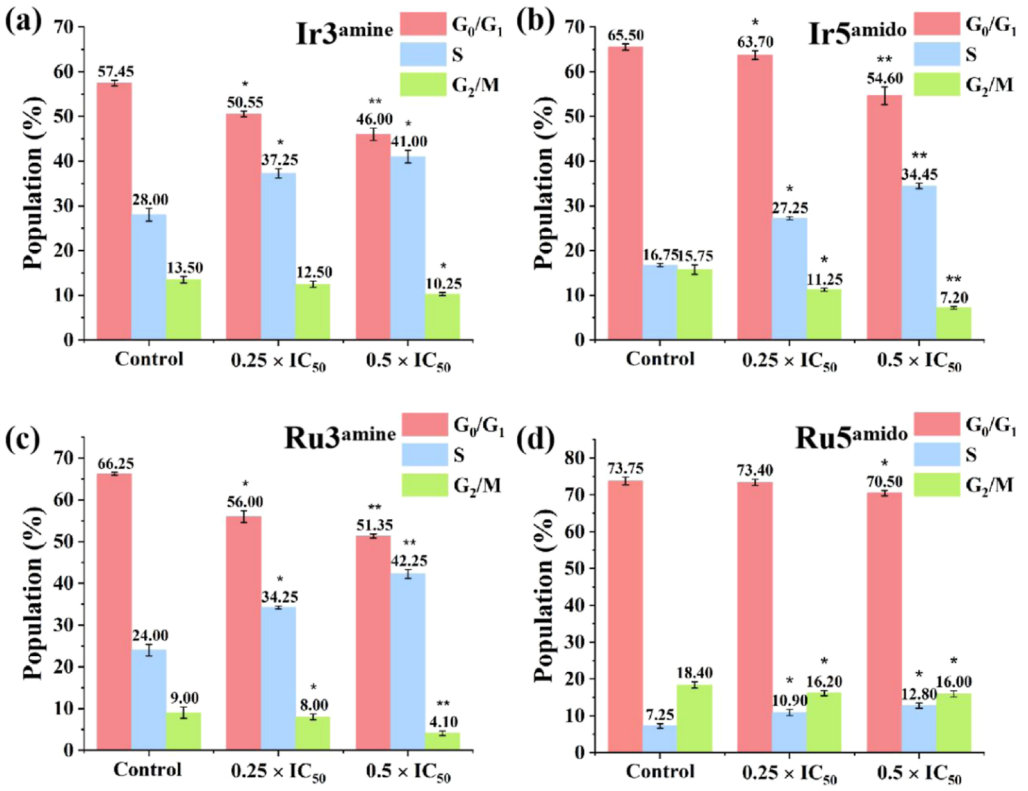

Figure 8. Cell cycle distribution of A549 cells treated with (a) **Ir3**^{amine}, (b) **Ir5**^{amido}, (c) **Ru3**^{amine}, and (d) **Ru5**^{amido} for 24 h at 0.25 × IC_{50} and 0.5 × IC_{50} concentrations was analyzed by flow cytometry using PI/RNase staining. Data are shown as mean ± SD from three replicates, with *p*-values calculated against the untreated control group (*p < 0.05, **p < 0.01).

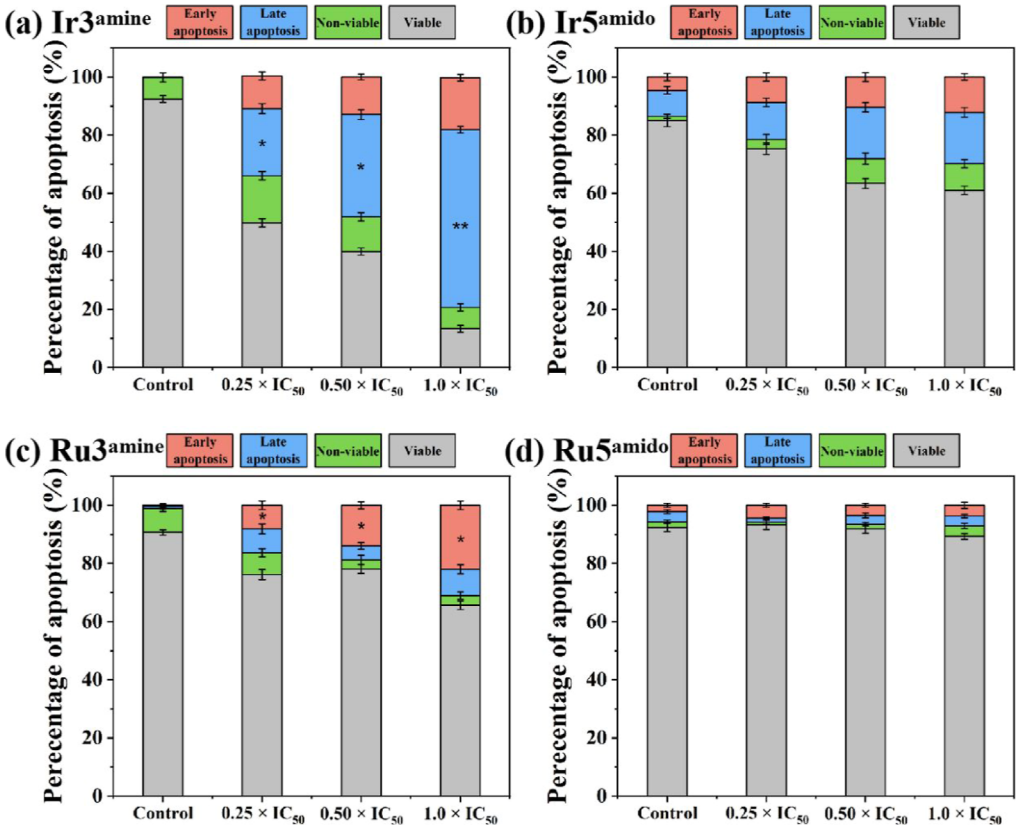

Figure 9. Apoptosis analysis and corresponding histograms for A549 cells treated with (a) **Ir3**^{amine}, (b) **Ir5**^{amido}, (c) **Ru3**^{amine}, and (d) **Ru5**^{amido} for 48 h at 37 °C. *p*-values were determined relative to the untreated control group (*p < 0.05, **p < 0.01).

https://doi.org/10.1021/acs.inorgchem.4c05599
Inorg. Chem. 2025, 64, 10379−10401

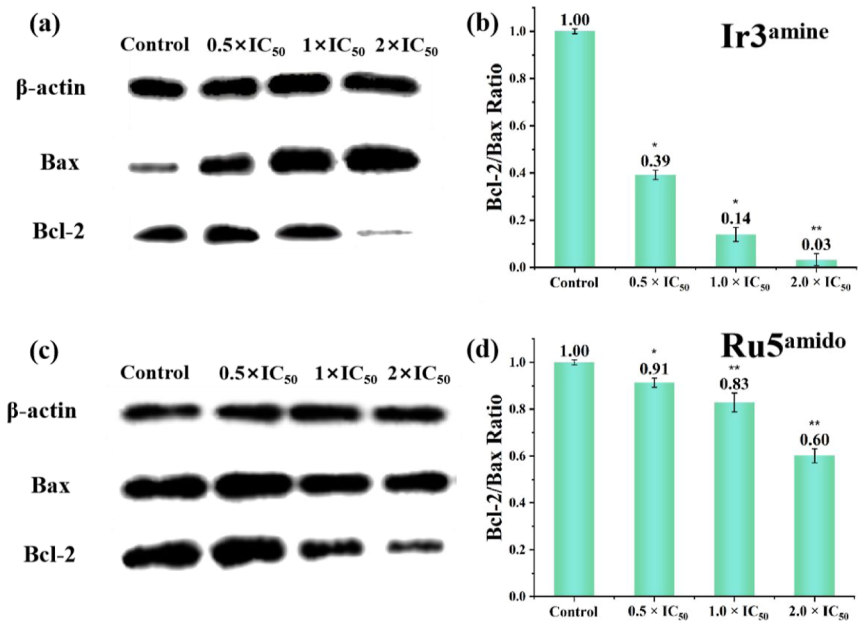

Figure 10. Protein expression levels analyzed by Western blot after 24 h treatment with (a) **Ir3**^{amine} and (c) **Ru5**^{amido} at concentrations of 0.5, 1.0, and 2.0 × IC_{50}. Histograms showing the changes of Bcl-2/Bax ratio levels at various (b) **Ir3**^{amine} and (d) **Ru5**^{amido} concentrations. Data represent the mean ± SD from three independent experiments. Statistical significance compared to the control: *p < 0.05, **p < 0.01.

function. The mitochondrial membrane potential (MMP, $\triangle\psi$m) is crucial for maintaining mitochondrial integrity and bioenergetics, and its loss (depolarization) is a key event in cell death pathways. A549 cancer cells were treated with **Ir3**^{amine}, **Ir5**^{amido}, **Ru3**^{amine}, and **Ru5**^{amido} at 0.5, 1.0, and 2.0 × IC_{50}, and their effects on MMP were evaluated by JC-1 staining and flow cytometry (Figures 7 and S84). Depolarization is indicated by a decrease in the red-to-green fluorescence ratio. The results showed a concentration-dependent mitochondrial dysfunction: as the drug concentration rose from 0.5 × IC_{50} to 2 × IC_{50}, the percentage of cells with depolarized mitochondria increased from 37.5%, 35.2%, 22.8%, and 28.7% to 82.2%, 86.3%, 70.5%, and 84.0%, respectively. Hence, these complexes may exert their anticancer effects by inducing mitochondrial dysfunction.

2.13. Cell-Cycle Arrest. The inhibition of cancer cell growth by anticancer drugs may arise from inducing cell cycle arrest, apoptosis, or a combination of these processes.[80,81] Thus, flow cytometric analysis was conducted to investigate whether the inhibition of cell growth was due to cell cycle arrest. Treatment with these complexes **Ir3**^{amine}, **Ir5**^{amido}, **Ru3**^{amine} and **Ru5**^{amido} at concentrations of 0.25 × IC_{50} and 0.5 × IC_{50} for 24 h resulted in a concentration-dependent increase in the S-phase cell population, with a corresponding reduction in the G_2/M and G_0/G_1 phases. At 0.5 × IC_{50}, the percentage of A549 cells in the S phase was elevated by 13.00% (**Ir3**^{amine}), 17.70% (**Ir5**^{amido}), 18.25% (**Ru3**^{amine}), and 5.55% (**Ru5**^{amido}) compared to the untreated control group (Figures 8 and S85–S88). These results demonstrate that both the pyridyl−amine and pyridyl−amido complexes primarily induce growth inhibition through S-phase cell cycle arrest, regardless of their coordination mode.

2.14. Apoptosis. Anticancer complexes producing high ROS levels can disturb the cellular redox balance, a process strongly linked to apoptosis induction and cellular damage.[82,83] To determine the apoptosis-inducing mechanism of cell death, an annexin V/PI assay was conducted. A549 cells were treated with **Ir3**^{amine}, **Ir5**^{amido}, **Ru3**^{amine}, and **Ru5**^{amido} at concentrations of 0.25, 0.5, and 1.0 × IC_{50}, and apoptosis was analyzed via flow cytometry (Figures 9 and S89–S92). Compared to the control group, both **Ir3**^{amine} and **Ru3**^{amine} significantly increased the percentage of apoptotic cells, with notable differences in early and late apoptosis. At 1.0 × IC_{50}, **Ir3**^{amine} induced apoptosis in 79.1% of A549 cells, with 17.9% attributed to early apoptosis and 61.2% to late apoptosis (Figure 9a). The late apoptotic population increased with concentration, while the early apoptotic population showed minimal changes between 0.5 and 1.0 × IC_{50}. For **Ru3**^{amine}, a total of 31.1% of cells underwent apoptosis at 1.0 × IC_{50}, consisting of 22.0% early and 9.1% late apoptosis (Figure 9c). Unlike **Ir3**^{amine}, **Ru3**^{amine} exhibited a concentration-dependent increase in the early apoptotic population as the concentration rose from 0.5 to 1.0 × IC_{50}. In contrast, **Ir5**^{amido} and **Ru5**^{amido} showed minimal changes in apoptotic cell populations across the tested concentrations, with results comparable to the control group and no clear concentration-dependent increase observed (Figure 9b,d). These results suggest that the pyridyl−amine complexes are capable of inducing apoptosis, whereas the pyridyl−amido complexes did not show any obvious apoptotic effect. Both types of complexes exhibit similar cytotoxicity, yet the pyridyl−amido complexes did not show obvious apoptotic effects. This discrepancy may suggest that apoptosis is not the primary mode of cell death for the pyridyl−amido complexes in A549 cells. Possible reasons include the differences in the mechanisms of action, like cell cycle arrest, which do not necessarily trigger classical apoptotic markers.

Within the Bcl-2 protein family, which plays a key role in apoptosis, the pro-apoptotic regulator Bax helps maintain the balance between cell survival and programmed death by downregulating Bcl-2. In this study, Western blot analysis was carried out to quantify Bax and Bcl-2 levels, aiming to determine whether both pyridyl−amine and pyridyl−amido complexes modulate apoptotic pathways (Figure 10). Notably, 18-electron pyridyl−amine complex **Ir3**^{amine} increased the Bcl-

https://doi.org/10.1021/acs.inorgchem.4c05599
Inorg. Chem. 2025, 64, 10379−10401

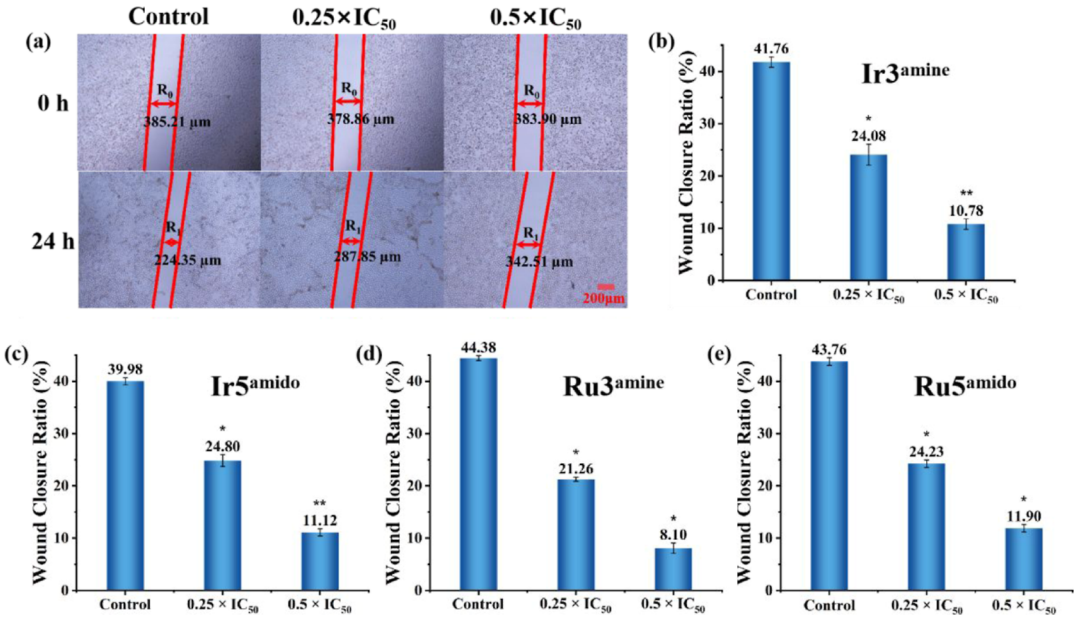

Figure 11. (a) Wound-healing assay showing A549 cells treated with Ir3amine for 24 h. (b–e) Histograms of A549 cells treated with **Ir3**^{amine}, **Ir5**^{amido}, **Ru3**^{amine}, and **Ru5**^{amido} for 24 h. Representative images were taken at 0 and 24 h, with wound widths indicated by lines (μm). Scale bar: 200 μm. Wound closure rate was calculated as $(R_0 - R_1)/R_0 \times 100\%$. Data are presented as mean ± SD from three replicates, with p-values compared to the untreated control group ($^*p < 0.05$, $^{**}p < 0.01$).

2/Bax ratio in A549 cells, suggesting that this effect contributes significantly to apoptosis, whereas 16-electron pyridyl–amido complex **Ru5**^{amido} did not significantly alter the Bcl-2/Bax ratio, further indicating a nonapoptotic mechanism of cell death. These observations align with the results of the apoptosis analysis described above (Figure 9).

2.15. Inhibition of Cell Migration. Inhibiting cancer cell migration is a key challenge in cancer therapy, as decreased surface adhesion allows malignant cells to detach from the primary tumor and spread to other parts of the body.[84,85] Cell migration, metastasis and invasion are closely associated with the breakdown of the extracellular matrix and the activity of cell adhesion molecules.[86,87] To assess the impact of **Ir3**^{amine}, **Ir5**^{amido}, **Ru3**^{amine}, and **Ru5**^{amido} on A549 cancer cell migration, a wound-healing experiment was performed (Figures 11 and S93–95). At 0.5 × IC_{50}, the wound closure rates (WCR) for cells treated with **Ir3**^{amine}, **Ir5**^{amido}, **Ru3**^{amine}, and **Ru5**^{amido} were significantly reduced to 10.78%, 11.12%, 8.10% and 11.90% respectively, compared to the control group values of 41.76%, 39.98%, 44.38% and 43.76%. Furthermore, all four complexes exhibited a concentration-dependent inhibitory effect on cell migration. These results demonstrate that both pyridyl–amine and pyridyl–amido complexes in this system effectively suppress the migration of A549 cancer cells in vitro.

3. CONCLUSIONS

This study systematically investigated the ligand- and metal-dependent coordination chemistry of iridium(III) and ruthenium(II) complexes synthesized from pyridyl–amine ligands. Ligand steric hindrance and metal centers were found to significantly influence their oxidation behavior and coordination modes. Smaller substituents, such as H and Me, facilitated oxidation to pyridyl–imine complexes under adventitious oxygen conditions, whereas bulkier substituents, such as *i*-Bu and mesityl, suppressed oxidation, stabilizing either pyridyl–amine or 16-electron pyridyl–amido complexes. Ruthenium(II) complexes exhibited higher resistance to oxidation compared to iridium(III) complexes, with moderate steric hindrance favoring stable pyridyl–amine complexes and extreme steric hindrance enabling the formation of pyridyl–amido 16-electron complexes. The aqueous stability of these newly synthesized complexes was confirmed. Most of the complexes demonstrated anticancer potency against A549 lung cancer, HeLa cervical cancer, and cisplatin-resistant A549/DDP cells. Interaction studies revealed weak binding affinities with CT-DNA, suggesting that DNA binding is not the primary mechanism of their anticancer potency. The further mechanistic investigations suggested a potential redox-driven pathway, where the catalytic conversion of NADH to NAD^+, elevated ROS levels and mitochondrial dysfunction may contribute to their anticancer activity. Pyridyl–amine complexes exhibited the ability to trigger apoptosis, whereas 16-electron pyridyl–amido complexes did not show a comparable apoptotic response. However, both types of complexes caused S-phase cell cycle arrest. In particular, wound-healing assays demonstrated that these complexes effectively inhibited A549 cell migration, indicating their potential to suppress cancer metastasis.

4. EXPERIMENTAL SECTION

Ligands **L1**, **L2**, **L4**, and **L5** were synthesized following established methods.[47,48] The preparation of bimetallic precursors **D1** and **D2** adhered to previously reported protocols.[88,89] Further experimental details, encompassing general methodologies and descriptions of biological assays, are presented in the Supporting Information. No uncommon hazards are noted.

4.1. Synthesis of Ligands.

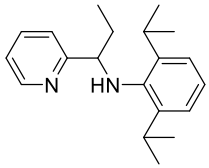

https://doi.org/10.1021/acs.inorgchem.4c05599
Inorg. Chem. 2025, 64, 10379–10401

4.1.1. L3. A solution of 2,6-diisopropyl-*N*-(pyridin-2-ylmethylene)-aniline (5.32 g, 20.00 mmol) in 100 mL of toluene was prepared, and triethylaluminum (30.00 mmol) was carefully added dropwise under nitrogen. The mixture was then heated at reflux for 12 h. After cooling, the reaction was quenched by adding 1 M NaOH solution while keeping it in an ice bath. The organic phase was washed with brine twice, then dried and filtered, and the solvent evaporated under reduced pressure. The product was recrystallized from hexane to afford white crystalline product. Yield: 3.84 g (64.9%).^{1}H NMR (500 MHz, $CDCl_3$): δ 8.63 (d, 1H), 7.44 (m, 1H), 7.23 (m, 1H), 7.15 (m, 1H), 7.09 (m, 1H), 6.96 (m, 1H), 6.86 (d, 1H), 4.08 (s, 1H, N*H*), 3.88 (m, 1H, C*H*CH_2CH_3), 3.23 (m, 2H, *i*-Pr−C*H*), 2.00 (m, 2H, CH_2CH_3), 1.21 (d, 6H, *i*-Pr−CH_3), 1.02 (d, 6H, *i*-Pr−CH_3), 0.78 (t, 3H, CH_2CH_3). ^{13}C NMR (126 MHz, $CDCl_3$): δ 162.02, 149.87, 141.86, 141.79, 135.86, 123.42, 123.28, 122.94, 122.08, 67.51 (NH−CH), 28.53(CH_2CH_3), 27.55 (*i*-Pr-CH), 24.25 (*i*-Pr-CH_3), 24.18 (*i*-Pr-CH_3), 11.15 (CH_2CH_3). ESI-MS (*m*/*z*): calcd for $C_{20}H_{29}N_2$, 297.2331; found, 297.2345, [M + H].

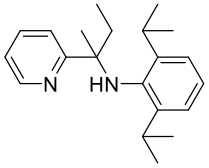

4.1.2. L6. A solution of 2,6-diisopropyl-*N*-(1-(2-pyridin)-ethylidene)benzenamine (5.60 g, 20.00 mmol) in 100 mL of toluene was prepared, and triethylaluminum (30.00 mmol) was carefully added dropwise under nitrogen. The mixture was then heated at reflux for 12 h. After cooling, the reaction was quenched by adding 1 M NaOH solution while keeping it in an ice bath. The organic phase was washed with brine twice, then dried and filtered, and the solvent evaporated under reduced pressure, yielding a clear, colorless oil as the final product. Yield: 3.56 g (57.4%). ^{1}H NMR (500 MHz, $CDCl_3$): δ 8.62 (s, 1H), 7.59 (m, 1H), 7.44 (d, 1H), 7.23 (t, 1H), 7.11 (m, 3H), 4.34 (s, 1H, N*H*), 3.10 (m, 2H, *i*-Pr−C*H*), 2.16 (m, 1H, CH_2CH_3), 1.94 (m, 1H, CH_2CH_3), 1.23 (s, 3H, CH_3), 1.11 (d, 6H, *i*-Pr−CH_3), 1.00 (d, 6H, *i*-Pr−CH_3), 0.68 (t, 3H, CH_2CH_3). ^{13}C NMR (126 MHz, $CDCl_3$): δ 166.76, 148.22, 146.64, 141.07, 135.94, 124.39, 122.94, 121.21, 120.52, 61.82 (NH−*C*), 38.56 (CH_2), 28.25 (*i*-Pr-CH), 24.13 (*i*-Pr-CH_3), 23.91 (*i*-Pr-CH_3), 22.69 (CH_3), 8.97 (CH_2CH_3). ESI-MS (*m*/*z*): calcd for $C_{21}H_{31}N_2$, 311.2487; found, 311.2491, [M + H].

4.2. Synthesis of Complexes. General method: A mixture of **D1**/**D2** (0.05 mmol, 1 equiv), pyridyl−amine ligands (0.10 mmol, 2 equiv), and NH_4PF_6 (0.20 mmol, 4 equiv) was prepared in methanol. The solution was stirred at room temperature for 24 h to ensure complete reaction. Afterward, the solvent was removed under reduced pressure, leaving a crude residue. This residue was dissolved in dichloromethane, filtered through a Celite pad, and the filtrate was treated with an excess of *n*-hexane to precipitate. The solid product was collected, thoroughly washed with *n*-hexane, and dried under vacuum to obtain the final complexes. (**Ir1**^{amine}, **Ir2**^{amine} and **Ir4**^{amido} have been reported in our previous work[47]).

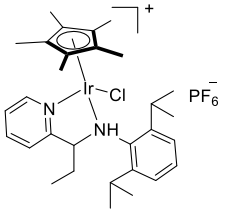

4.2.1. Ir3^{amine}. Orange powder. Yield 50.5 mg (62.8%). ^{1}H NMR (500 MHz, $CDCl_3$): δ 8.64 (d, 1H), 8.01 (t, 1H), 7.60 (t, 1H), 7.44 (d, 1H), 7.36 (m, 1H), 7.29 (m, 2H), 7.12 (m, 1H, N*H*), 5.36 (m, 1H, C*H*−N), 3.50 (m, 1H, *i*-Pr−CH_3), 2.86 (m, 1H, *i*-Pr−C*H*), 2.08 (m, 1H, CH_2), 1.99 (m, 1H, CH_2), 1.44 (d, 3H, *i*-Pr−CH_3), 1.39 (s, 15H, Cp*−CH_3), 1.37 (s, 3H, *i*-Pr−CH_3), 1.31 (d, 3H, *i*-Pr−CH_3), 1.26 (d, 3H, *i*-Pr−CH_3), 0.86 (t, 3H, CH_2CH_3). ^{13}C NMR (126 MHz, $CDCl_3$): δ 162.99, 151.39, 141.30, 141.06, 139.71, 139.21, 88.96 (C_5Me_5), 72.12 (*N*−CH), 28.45 (*i*-Pr-CH), 27.69 (*i*-Pr-CH), 27.62 (CH_2CH_3), 26.70 (*i*-Pr-CH_3), 26.02 (*i*-Pr-CH_3), 25.68 (*i*-Pr-CH_3), 24.49 (*i*-Pr-CH_3), 9.96 (CH_2CH_3), 8.60 (Cp*-CH_3). ESI-MS (*m*/*z*): calcd for $C_{30}H_{43}ClIrN_2$, 659.2744; found, 659.2714, [M-PF_6]$^+$. Elemental analysis: calcd for $C_{30}H_{43}ClF_6IrN_2P$: C, 44.80; H, 5.39; N, 3.48. Found: C, 44.92; H, 5.37; N, 3.49.

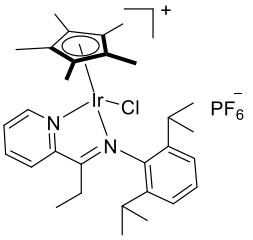

4.2.2. Ir3^{imine}. First, pyridyl−amine **Ir3**^{amine} was synthesized by the general method, followed by the formation of the pyridyl−imine complex **Ir3**^{imine} via gradual oxidation (14 days) during the cultivation of single crystal. Red flaky crystals. Yield 46.4 mg (57.8%). ^{1}H NMR (500 MHz, $CDCl_3$): δ 8.91 (d, 1H), 8.21 (d, 2H), 7.96 (m, 1H), 7.33 (m, 3H), 3.44 (m, *i*-Pr−C*H*), 3.03 (m, 1H, *i*-Pr−C*H*), 2.63 (m, 1H, CH_2), 2.49 (m, 1H, CH_2), 1.44 (s, 15H, Cp*−CH_3), 1.37 (d, 3H, *i*-Pr−CH_3), 1.27 (d, 3H, CH_2CH_3), 1.22 (d, 3H, *i*-Pr−CH_3), 1.15 (d, 3H, *i*-Pr−CH_3), 0.95 (d, 3H, *i*-Pr−CH_3). ^{13}C NMR (126 MHz, $CDCl_3$): δ 171.67 (C═N), 152.24, 151.05, 148.12, 144.41, 142.66, 139.57, 129.55, 129.18, 124.74, 124.05, 99.99, 91.03 (C_5Me_5), 27.82 (*i*-Pr-CH_3), 27.61 (*i*-Pr-CH), 27.58 (CH_2CH_3), 26.57 (*i*-Pr-CH_3), 26.00 (*i*-Pr-CH_3), 23.72 (*i*-Pr-CH_3), 21.63 (*i*-Pr-CH_3), 13.75 (CH_2CH_3), 8.51 (Cp*-CH_3). ESI-MS (*m*/*z*): calcd for $C_{30}H_{41}ClIrN_2$, 657.2588; found, 657.2576, [M-PF_6]$^+$. Elemental analysis: calcd for $C_{30}H_{41}ClF_6IrN_2P$: C, 44.91; H, 5.15; N, 3.49. Found: C, 44.81; H, 5.17; N, 3.48.

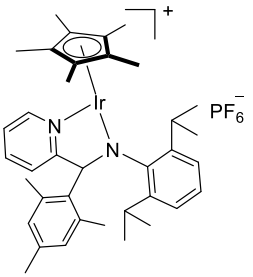

4.2.3. Ir5^{amido}. Red powder. Yield 50.2 mg (58.5%). ^{1}H NMR (500 MHz, $CDCl_3$): δ 9.19 (d, 1H), 7.84 (m, 2H), 7.20 (m, 2H), 7.10 (d, 1H), 7.01 (d, 1H), 6.68 (s, 1H), 6.54 (s, 1H), 4.90 (s, 1H, C*H*−N), 3.11 (m, 1H, *i*-Pr−C*H*), 2.76 (m, 1H, *i*-Pr−C*H*), 2.14 (s, 3H, Ar−CH_3), 1.69 (s, 15H, Cp*-CH_3), 1.65 (s, 3*H*, Ar−CH_3), 1.40 (s, 3H, Ar−CH_3), 1.31 (d, 3H, *i*-Pr−CH_3), 1.28 (d, 3H, *i*-Pr−CH_3), 1.22 (d, 3H, *i*-Pr−CH_3), −0.15 (d, 3H, *i*-Pr−CH_3). ^{13}C NMR (126 MHz, $CDCl_3$): δ 169.75, 150.47, 150.15, 144.21, 143.71, 139.31, 139.11, 138.95, 138.87, 132.84, 129.98, 128.81, 127.17, 125.64, 124.67, 124.08, 122.34, 89.66 (C_5Me_5), 86.21 (CH), 27.31 (Ar−CH_3), 27.19 (Ar−CH_3), 26.16 (*i*-Pr-CH), 23.81 (*i*-Pr-CH), 21.34 (*i*-Pr-CH_3), 20.62 (*i*-Pr-CH_3), 18.64 (*i*-Pr-CH_3), 9.46 (Cp*-CH_3). ESI-MS (*m*/*z*): calcd for $C_{37}H_{48}IrN_2$, 713.3447; found, 713.3437, [M-PF_6]$^+$. Elemental analysis: calcd for $C_{37}H_{48}F_6IrN_2P$: C, 51.80; H, 5.64; N, 3.27. Found: C, 51.95; H, 5.62; N, 3.26.

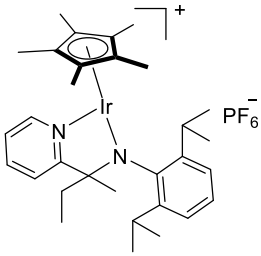

https://doi.org/10.1021/acs.inorgchem.4c05599
Inorg. Chem. 2025, 64, 10379−10401

4.2.4. Ir6^{amido}. Red powder. Yield 47.5 mg (60.7%). ^{1}H NMR (500 MHz, $CDCl_3$): δ 9.10 (d, 1H), 8.05 (t, 1H), 7.78 (t, 1H), 7.58 (d, 1H), 7.25 (d, 1H), 7.16 (t, Hz, 2H), 3.04 (m, 1H, *i*-Pr−C*H*), 2.51 (m, 1H, *i*-Pr−C*H*), 1.93 (m, 1H, CH_2CH$_3$), 1.68 (m, 1H, CH_2CH$_3$), 1.60 (s, 15H, Cp*−CH_3), 1.48 (d, 3H, *i*-Pr−CH_3), 1.35 (s, 3H, CH_3), 1.27 (d, 3H, *i*-Pr−CH_3), 1.13 (d, 3H, *i*-Pr−CH_3), 0.96 (d, 3H, *i*-Pr−CH_3), 0.28 (t, 3H, CH$_2$CH_3). ^{13}C NMR (126 MHz, $CDCl_3$): δ 169.90, 151.32, 148.71, 146.16, 143.45, 139.75, 126.94, 125.92, 124.69, 123.97, 120.35, 89.27 (*C*$_5$Me$_5$), 85.18 (*N*−*C*), 39.71 (CH$_2$), 29.03 (*C*H$_3$), 28.16 (*i*-Pr-*C*H), 27.43 (*i*-Pr-CH), 25.99 (*i*-Pr-*C*H$_3$), 25.87 (*i*-Pr-CH$_3$), 24.55 (*i*-Pr-CH$_3$), 23.19 (*i*-Pr-CH$_3$), 9.88(Cp*-*C*H$_3$), 9.75 (CH$_2$*C*H$_3$). ESI-MS (*m*/*z*): calcd for $C_{31}H_{45}IrN_2$, 637.3134; found, 637.3144, [M-PF$_6$]$^+$. Elemental analysis: calcd for $C_{31}H_{44}F_6IrN_2P$: C, 47.62; H, 5.67; N, 3.58. Found: C, 47.52; H, 5.69; N, 3.57.

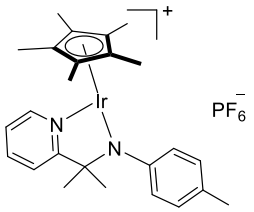

4.2.5. Ir7^{amido}. Red powder. Yield 40.3 mg (57.7%). ^{1}H NMR (500 MHz, CDCl3): δ 9.02 (d, 1H), 8.04 (t, 1H), 7.75 (m, 1H), 7.63 (d, 1H), 7.26 (d, 2H), 6.84 (d, 2H), 2.46 (s, 3H, Ar−CH_3), 1.57 (s, 15H, Cp*−CH_3), 1.46 (s, 6H, CH_3). Due to the limited solubility of this complex, ^{13}C NMR spectroscopy was not performed. ESI-MS (*m*/*z*): calcd for $C_{25}H_{32}IrN_2$, 553.2195; found, 553.2179, [M-PF$_6$]$^+$. Elemental analysis: calcd for $C_{25}H_{32}F_6IrN_2P$: C, 43.04; H, 4.62; N, 4.02. Found: C, 43.16; H, 4.60; N, 4.03.

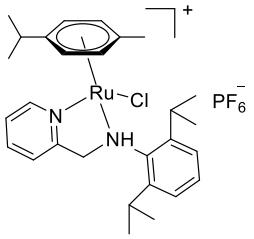

4.2.6. Ru1^{amine}. Yellow powder. Using the general method, a combination of pyridyl−imine and pyridyl−amine complexes was initially obtained. To isolate the pure pyridyl−amine complex **Ru1^{amine}**, the reaction duration was reduced to 2 h, ensuring minimal oxidation and yielding the desired product without contamination from the oxidized pyridyl−imine species. Yield 42.2 mg (61.7%). ^{1}H NMR (500 MHz, $CDCl_3$): δ 9.36 (d, 1H), 7.92 (t, 1H), 7.71 (t, 1H), 7.38 (m, 2H), 7.28 (d, 2H), 6.80 (m, 1H, N*H*), 5.85 (d, 1H), 5.58 (d, 1H), 5.10 (q, 2H), 4.59 (m, 1H, CH_2), 4.40 (m, 1H, CH_2), 3.40 (m, 1H, *i*-Pr−C*H*), 2.87 (m, 1H, *i*-Pr−C*H*), 2.74 (m, 1H, *i*-Pr−C*H*), 1.99 (s, 3H, Ar−CH_3), 1.52 (d, 3H, *i*-Pr−CH_3), 1.44 (d, 3H, *i*-Pr−CH_3), 1.33 (d, 3H, *i*-Pr−CH_3), 1.23 (d, 3H, *i*-Pr−CH_3), 1.21 (m, 6H, *i*-Pr−CH_3). ^{13}C NMR (126 MHz, $CDCl_3$): δ 159.71, 154.52, 142.38, 139.88, 139.03, 138.07, 127.30, 126.26, 125.82, 123.22, 120.07, 104.35, 98.67, 83.25, 83.11, 82.87, 80.72, 59.95 (CH$_2$), 29.76 (Ar-*i*-Pr-CH), 27.82 (*i*-Pr-CH), 27.26 (*i*-Pr-CH), 25.07 (*i*-Pr-CH$_3$), 24.82 (*i*-Pr-CH$_3$), 24.51 (*i*-Pr-CH$_3$), 21.58 (*i*-Pr-CH$_3$), 21.11 (Ar-*i*-Pr-CH$_3$), 21.07 (Ar-*i*-Pr-CH$_3$), 16.28 (Ar-CH$_3$). ESI-MS (*m*/*z*): calcd for $C_{28}H_{38}ClN_2Ru$, 539.1767; found, 539.1685, [M-PF$_6$]$^+$. Elemental analysis: calcd for $C_{28}H_{38}ClF_6N_2PRu$: C, 49.16; H, 5.60; N, 4.09. Found: C, 49.25; H, 5.58; N, 4.08.

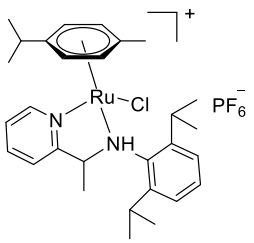

4.2.7. Ru2^{amine}. Yellow powder. Yield 42.9 mg (61.4%). ^{1}H NMR (500 MHz, $CDCl_3$): δ 9.17 (d, 1H), 7.97 (t, 1H), 7.63 (t, 1H), 7.42 (m, 1H), 7.37 (m, 2H), 7.30 (m, 1H), 6.18 (m, 1H, C*H*−N), 5.79 (d, 1H), 5.54 (d, 1H), 5.26 (d, 1H), 5.19 (m, 2H, Ar *p*-cymene (1H)+N*H* (1H)), 3.39 (m, 2H, *i*-Pr−C*H*), 2.64 (m, 1H, *i*-Pr−C*H*), 2.09 (s, 3H, Ar−CH_3), 1.63 (d, 3H, CHCH_3), 1.46 (d, 3H, *i*-Pr−CH_3), 1.38 (d, 3H, *i*-Pr−CH_3), 1.35 (d, 3H, *i*-Pr−CH_3), 1.22 (d, 3H, *i*-Pr−CH_3), 1.17 (d, 3H, *i*-Pr−CH_3), 0.91 (d, 3H, *i*-Pr−CH_3). ^{13}C NMR (126 MHz, $CDCl_3$): δ 162.06, 155.02, 141.44, 141.05, 140.25, 140.09, 128.15, 126.86, 126.49, 125.63, 122.76, 103.70, 100.20, 85.26, 85.12, 82.84, 82.02, 66.26 (CH), 30.23 (Ar-*i*-Pr-CH), 29.17 (*i*-Pr-CH), 28.32 (*i*-Pr-CH), 26.20 (*i*-Pr-CH$_3$), 25.45 (*i*-Pr-CH$_3$), 25.29 (*i*-Pr-CH$_3$), 24.53 (*i*-Pr-CH$_3$), 22.32 (Ar-*i*-Pr-CH$_3$), 21.95 (Ar-*i*-Pr-CH$_3$), 20.47 (Ar-CH$_3$), 17.73 (CHCH$_3$). ESI-MS (*m*/*z*): calcd for $C_{29}H_{40}ClF_6N_2Ru$, 553.1924; found, 553.1896, [M-PF$_6$]$^+$. Elemental analysis: calcd for $C_{29}H_{40}ClF_6N_2PRu$: C, 49.89; H, 5.78; N, 4.01. Found: C, 50.01; H, 5.76; N, 4.02.

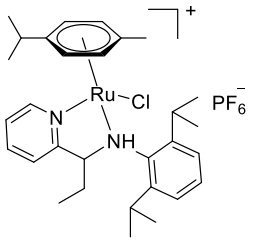

4.2.8. Ru3^{amine}. Yellow powder. Yield 43.5 mg (61.1%). ^{1}H NMR (500 MHz, $CDCl_3$): δ 9.21 (s, 1H), 7.97 (s, 1H), 7.66 (s, 1H), 7.39 (m, 2H), 7.31 (d, 1H), 6.41 (m, 1H, C*H*−N), 5.66 (d, 1H), 5.50 (d, 1H), 5.28 (d, 1H), 5.20 (m, 1H, N*H*), 5.08 (s, 1H), 3.44 (m, 1H, *i*-Pr−C*H*), 3.31 (m, 1H, *i*-Pr−C*H*), 2.68 (m, 1H, *i*-Pr−C*H*), 2.06 (s, 3H, Ar−CH_3), 1.77 (m, 2H, CH_2), 1.60 (d, 3H, *i*-Pr−CH_3), 1.40 (d, 3H, *i*-Pr−CH_3), 1.38 (d, 3H, *i*-Pr−CH_3), 1.21 (d, 3H, *i*-Pr−CH_3), 1.19 (d, 3H, *i*-Pr−CH_3), 0.97 (d, 3H, *i*-Pr−CH_3), 0.72 (t, 3H, CH$_2$CH_3). ^{13}C NMR (126 MHz, $CDCl_3$): δ 160.79, 155.27, 141.44, 140.88, 140.78, 139.56, 128.04, 127.01, 126.42, 125.89, 122.98, 104.55, 100.62, 85.05, 83.86, 83.02, 82.37, 70.90 (CH), 30.26 (Ar-*i*-Pr-CH), 29.25 (*i*-Pr-CH), 28.36 (*i*-Pr-CH), 26.48 (CH$_2$CH$_3$), 25.68 (*i*-Pr-CH$_3$), 25.05 (*i*-Pr-CH$_3$), 24.96 (*i*-Pr-CH$_3$), 22.62 (*i*-Pr-CH$_3$), 21.93 (Ar-*i*-Pr-CH$_3$), 17.86 (Ar-*i*-Pr-CH$_3$), 8.76 (Ar-CH$_3$), 1.02 (CH$_2$CH$_3$). ESI-MS (*m*/*z*): calcd for $C_{30}H_{42}ClN_2Ru$, 567.2080; found, 567.2059, [M-PF$_6$]$^+$. Elemental analysis: calcd for $C_{30}H_{42}ClF_6N_2PRu$: C, 50.60; H, 5.94; N, 3.93. Found: C, 50.71; H, 5.92; N, 3.94.

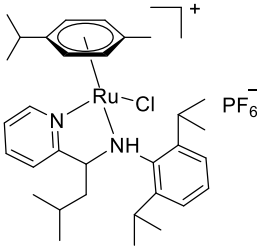

4.2.9. Ru4^{amine}. Yellow powder. Yield 50.8 mg (68.6%). ^{1}H NMR (500 MHz, $CDCl_3$): δ 9.40 (d, 1H), 7.97 (t, 1H), 7.73 (t, 1H), 7.38 (d, 2H), 7.32 (m, 1H), 7.20 (d, 1H), 6.28 (d, 1H, C*H*−N), 5.66 (d, 1H), 5.45 (d, 1H), 5.21 (d, 1H), 5.14 (d, 1H), 4.63 (m, 1H, CH$_2$C*H*(CH$_3$)$_2$), 3.36 (m, 1H, *i*-Pr−C*H*), 2.88 (m, 1H, *i*-Pr−C*H*), 2.71 (m, 1H, *i*-Pr−C*H*), 1.96 (s, 3H, Ar−CH_3), 1.79 (m, 2H, CH_2), 1.53 (d, 3H, *i*-Pr−CH_3), 1.46 (d, 3H, *i*-Pr−CH_3), 1.38 (d, 3H, *i*-Pr−CH_3), 1.35 (m, 6H, CH$_2$CH(CH_3)$_2$), 1.18 (d, 3H, *i*-Pr−CH_3), 0.75 (d, 3H, *i*-Pr−CH_3), 0.72 (d, 3H, *i*-Pr−CH_3). ^{13}C NMR (126 MHz, $CDCl_3$): δ 164.96, 155.37, 143.93, 139.87, 139.81, 139.22, 128.10, 127.62, 126.31, 125.36, 121.87, 106.74, 99.54, 84.64, 83.80, 82.52, 81.87, 71.25 (CH), 49.91 (CH$_2$), 30.88 (Ar-*i*-Pr-CH), 28.97 (*i*-Pr-CH), 28.19 (*i*-Pr-CH), 26.89 (CH$_2$CH(CH$_3$)$_2$), 25.81 (*i*-Pr-CH$_3$), 25.43 (CH$_2$CH(CH$_3$)$_2$), 25.02 (*i*-Pr-CH$_3$), 23.37 (*i*-Pr-CH$_3$), 22.50 (*i*-Pr-CH$_3$), 21.81 (Ar-*i*-Pr-CH$_3$), 21.72 (Ar-*i*-Pr-CH$_3$), 16.98 (Ar-

https://doi.org/10.1021/acs.inorgchem.4c05599
Inorg. Chem. 2025, 64, 10379−10401

CH_3). ESI-MS (m/z): calcd for $C_{32}H_{46}N_2Ru$, 559.2626; found, 559.2659, $[M\text{-}HCl\text{-}PF_6]^+$. Elemental analysis: calcd for $C_{32}H_{47}ClF_6N_2PRu$: C, 51.92; H, 6.26; N, 3.78. Found: C, 51.80; H, 6.28; N, 3.77.

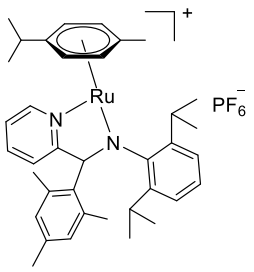

4.2.10. Ru5^{amido}. Purple powder. Yield 46.7 mg (60.9%). ^{1}H NMR (500 MHz, $CDCl_3$): δ 10.07 (d, 1H), 7.71 (dt, 2H), 7.21 (d, 1H), 7.02 (d, 1H), 6.82 (d, 1H), 6.63 (s, 1H, C*H*−N), 6.52 (s, 1H), 6.02 (d, 1H), 5.79 (d, 1H), 5.52 (s, 2H), 4.75 (s, 1H), 3.01 (m, 2H, *i*-Pr−C*H*), 2.70 (m, 1H, *i*-Pr−C*H*), 2.20 (s, 3H, Ar−CH_3), 2.12 (s, 3H, Ar−CH_3), 1.58 (s, 3H, Ar−CH_3), 1.38 (d, 3H, *i*-Pr−CH_3), 1.33 (d, 3H, *i*-Pr−CH_3), 1.31 (d, 6H, *i*-Pr−CH_3), 1.28 (m, 6H, *i*-Pr−CH_3 (3H)+Ar−CH_3 (3H)), −0.08 (d, 3H, *i*-Pr−CH_3). ^{13}C NMR (126 MHz, $CDCl_3$): δ 167.69, 154.13, 142.40, 142.35, 139.04, 138.91, 138.85, 138.70, 132.46, 129.96, 127.74, 127.22, 124.77, 124.63, 124.30, 121.62, 101.36, 92.27, 86.38, 84.34, 83.52, 82.27, 81.34 (CH), 31.44 (Ar-*i*-Pr-CH), 27.91 (*i*-Pr-CH), 27.89 (*i*-Pr-CH), 27.49 (*i*-Pr-CH_3), 27.36 (*i*-Pr-CH_3), 25.50 (*i*-Pr-CH_3), 23.42 (*i*-Pr-CH_3), 23.40 (Ar-*i*-Pr-CH_3), 23.03 (Ar-*i*-Pr-CH_3), 21.44 (Ar−CH_3), 20.58 (Ar-CH_3), 19.81 (Ar−CH_3), 18.74 (Ar−CH_3). ESI-MS (m/z): calcd for $C_{37}H_{47}N_2Ru$, 621.2783; found, 621.2872, $[M\text{-}PF_6]^+$. Elemental analysis: calcd for $C_{37}H_{47}F_6N_2PRu$: C, 58.03; H, 6.19; N, 3.66. Found: C, 58.15; H, 6.16; N, 3.67.

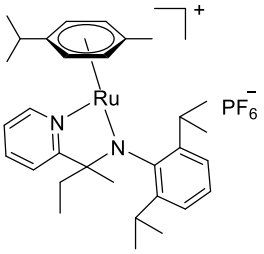

4.2.11. Ru6^{amido}. Purple powder. Yield 44.5 mg (64.5%).^{1}H NMR (500 MHz, $CDCl_3$): δ 9.62 (d, 1H), 7.65 (t, 1H), 7.49 (t, 1H), 6.98 (d, 1H), 6.93 (m, 1H), 5.58 (d, 1H), 5.52 (d, 1H), 5.31 (d, 1H), 5.29 (d, 1H), 3.19 (m, 1H, *i*-Pr−C*H*), 2.66 (m, 1H, *i*-Pr−C*H*), 2.05 (m, 1H, *i*-Pr−C*H*), 1.42 (m, 1H, CH_2CH_3), 1.35 (m, 6H, *i*-Pr−CH_3), 1.27 (m, 1H, CH_2CH_3), 1.09 (s, 3H, Ar−CH_3), 1.07 (d, 6H, *i*-Pr−CH_3), 1.00 (s, 3H, CH_3), 0.97 (d, 3H, *i*-Pr−CH_3), 0.86 (d, 3H, *i*-Pr−CH_3), 0.01 (t, 3H, CH_2CH_3). ^{13}C NMR (126 MHz, $CDCl_3$): δ 167.57, 155.02, 151.73, 144.69, 141.74, 139.09, 127.05, 124.99, 124.69, 124.57, 120.22, 104.98, 93.29, 86.17, 83.84, 81.79, 79.03, 78.99 (*N*−*C*), 39.49 (Ar- *i*-Pr-CH), 31.32 (CH_2), 28.75 (CH_3), 27.71 (*i*-Pr-CH), 26.95 (*i*-Pr-CH), 26.89 (*i*-Pr-CH_3), 26.51 (*i*-Pr-CH_3), 24.33 (*i*-Pr-CH_3), 24.05 (*i*-Pr-CH_3), 23.14 (Ar-*i*-Pr-CH_3), 22.78 (Ar-*i*-Pr-CH_3), 17.60 (Ar-CH_3), 9.70 (CH_2CH_3). ESI-MS (m/z): calcd for $C_{31}H_{43}N_2Ru$, 545.2470; found, 545.2479, $[M\text{-}PF_6]^+$. Elemental analysis: calcd for $C_{31}H_{43}F_6N_2PRu$: C, 53.98; H, 6.28; N, 4.06. Found: C, 53.89; H, 6.30; N, 4.05.

■ ASSOCIATED CONTENT

Supporting Information

The Supporting Information is available free of charge at https://pubs.acs.org/doi/10.1021/acs.inorgchem.4c05599.

Additional experimental details and methods, ^{1}H and ^{13}C {^{1}H}NMR spectra, and ESI-MS spectra for all compounds, experimental images and biological experiment data (Figures S1−S95, and Tables S1−S16) (PDF)

Accession Codes

CCDC 2396390 (**Ir3^{amine}**), 2396393 (**Ir3^{imine}**), 2396396 (**Ir5^{amido}**), 2409367 (**Ir7^{amido}**), 2396392 (**Ru1^{amine}**), 2396391 (**Ru2^{amine}**), 2396395 (**Ru4^{amine}**) and 2396394 (**Ru5^{amido}**) contain the supplementary crystallographic data for this paper. These data can be obtained free of charge via www.ccdc.cam.ac.uk/data_request/cif, or by emailing data_request@ccdc.cam.ac.uk, or by contacting The Cambridge Crystallographic Data Centre, 12 Union Road, Cambridge CB2 1EZ, UK; fax: +44 1223 336033.

■ AUTHOR INFORMATION

Corresponding Authors

Lihua Guo − *Key Laboratory of Life-Organic Analysis of Shandong Province, Key Laboratory of Green Natural Products and Pharmaceutical Intermediates in Colleges and Universities of Shandong Province, School of Chemistry and Chemical Engineering, Qufu Normal University, Qufu 273165, P. R. China;* orcid.org/0000-0002-0842-9958; Email: guolihua@qfnu.edu.cn

Zhe Liu − *Key Laboratory of Life-Organic Analysis of Shandong Province, Key Laboratory of Green Natural Products and Pharmaceutical Intermediates in Colleges and Universities of Shandong Province, School of Chemistry and Chemical Engineering, Qufu Normal University, Qufu 273165, P. R. China;* orcid.org/0000-0001-5796-4335; Email: liuzheqd@163.com

Authors

Zhihao Yang − *Key Laboratory of Life-Organic Analysis of Shandong Province, Key Laboratory of Green Natural Products and Pharmaceutical Intermediates in Colleges and Universities of Shandong Province, School of Chemistry and Chemical Engineering, Qufu Normal University, Qufu 273165, P. R. China*

Heqian Dong − *Key Laboratory of Life-Organic Analysis of Shandong Province, Key Laboratory of Green Natural Products and Pharmaceutical Intermediates in Colleges and Universities of Shandong Province, School of Chemistry and Chemical Engineering, Qufu Normal University, Qufu 273165, P. R. China*

Kangning Lai − *Key Laboratory of Life-Organic Analysis of Shandong Province, Key Laboratory of Green Natural Products and Pharmaceutical Intermediates in Colleges and Universities of Shandong Province, School of Chemistry and Chemical Engineering, Qufu Normal University, Qufu 273165, P. R. China*

Hanxiu Fu − *Key Laboratory of Life-Organic Analysis of Shandong Province, Key Laboratory of Green Natural Products and Pharmaceutical Intermediates in Colleges and Universities of Shandong Province, School of Chemistry and Chemical Engineering, Qufu Normal University, Qufu 273165, P. R. China*

Yuwen Gong − *Key Laboratory of Life-Organic Analysis of Shandong Province, Key Laboratory of Green Natural Products and Pharmaceutical Intermediates in Colleges and Universities of Shandong Province, School of Chemistry and Chemical Engineering, Qufu Normal University, Qufu 273165, P. R. China*

Susu Li − *Key Laboratory of Life-Organic Analysis of Shandong Province, Key Laboratory of Green Natural*

Products and Pharmaceutical Intermediates in Colleges and Universities of Shandong Province, School of Chemistry and Chemical Engineering, Qufu Normal University, Qufu 273165, P. R. China

Mingbo Yue − *Key Laboratory of Life-Organic Analysis of Shandong Province, Key Laboratory of Green Natural Products and Pharmaceutical Intermediates in Colleges and Universities of Shandong Province, School of Chemistry and Chemical Engineering, Qufu Normal University, Qufu 273165, P. R. China;* orcid.org/0000-0002-8534-7606

Complete contact information is available at: https://pubs.acs.org/10.1021/acs.inorgchem.4c05599

Notes

The authors declare no competing financial interest.

■ ACKNOWLEDGMENTS

We gratefully acknowledge the support provided by the Taishan Scholars Program and the Young Talents Invitation Program of Shandong Provincial Colleges and Universities. We also extend our thanks to Shiyanjia Lab (www.shiyanjia.com) for conducting the single-crystal XRD data analysis.

■ REFERENCES

(1) Wang, D.; Lippard, S. J. Cellular processing of platinum anticancer drugs. *Nat. Rev. Drug Discov.* **2005**, *4*, 307−320.

(2) Rosenberg, B.; Van Camp, L.; Krigas, T. S. Inhibition of Cell Division in Escherichia coli by Electrolysis Products from a Platinum Electrode. *Nature* **1965**, *205*, 698−699.

(3) Kelland, L. The resurgence of platinum-based cancer chemotherapy. *Nat. Rev. Cancer* **2007**, *7*, 573−584.

(4) Xu, F. J.; Liu, R. S.; Biao, L. H.; Zu, Y. G.; Liu, Z. G. Study on the interactions between anti-cancer drug oxaliplatin and DNA. *Prog. Biochem. Biophys.* **2016**, *43*, 684−690.

(5) Liu, F. F.; Gou, S. H.; Chen, F. H.; Fang, L.; Zhao, J. Study on antitumor platinum(II) complexes of chiral diamines with dicyclic species as steric hindrance. *J. Med. Chem.* **2015**, *58*, 6368−6377.

(6) Wang, Z. M.; Yu, H. Y.; Gou, S. H.; Chen, F. H.; Fang, L. Design, synthesis, and biological features of platinum(II) complexes with rigid steric hindrance. *Inorg. Chem.* **2016**, *55*, 4519−4528.

(7) Wang, X. H.; Wang, X. Y.; Jin, S. X.; Muhammad, N.; Guo, Z. J. Stimuli-responsive therapeutic metallodrugs. *Chem. Rev.* **2019**, *119*, 1138−1192.

(8) Florea, A.-M.; Busselberg, D. Cisplatin as an anti-tumor drug: cellular mechanisms of activity, drug resistance and induced side effects. *Cancers* **2011**, *3*, 1351−1371.

(9) Vock, C. A.; Ang, W. H.; Scolaro, C.; Phillips, A. D.; Lagopoulos, L.; Juillerat-Jeanneret, L.; Sava, G.; Scopelliti, R.; Dyson, P. J. Development of ruthenium antitumor drugs that overcome multidrug resistance mechanisms. *J. Med. Chem.* **2007**, *50*, 2166−2175.

(10) Zhao, J.; Zhang, D. Y.; Hua, W. Y.; Li, W. C.; Xu, G.; Gou, S. H. Anticancer activity of bifunctional organometallic Ru(II) arene complexes containing a 7-hydroxycoumarin group. *Organometallics* **2018**, *37*, 441−447.

(11) Qin, W. W.; Pan, Z. Y.; Cai, D. H.; Li, Y.; He, L. Cyclometalated iridium(III) complexes for mitochondria-targeted combined chemo-photodynamic therapy. *Dalton Trans.* **2020**, *49*, 3562−3569.

(12) Hildebrandt, J.; Häfner, N.; Kritsch, D.; Görls, H.; Dürst, M.; Runnebaum, I. B.; Weigand, W. Highly cytotoxic osmium(II) compounds and their ruthenium(II) analogues targeting ovarian carcinoma cell lines and evading cisplatin resistance mechanisms. *Int. J. Mol. Sci.* **2022**, *23*, 4976.

(13) Cunha, B. N.; Luna-Dulcey, L.; Plutin, A. M.; Silveira, R. G.; Honorato, J.; Cairo, R. R.; de Oliveira, T. D.; Cominetti, M. R.; Castellano, E. E.; Batista, A. A. Selective coordination mode of acylthiourea ligands in half-sandwich Ru(II) complexes and their cytotoxic evaluation. *Inorg. Chem.* **2020**, *59*, 5072−5085.

(14) Habtemariam, A.; Melchart, M.; Fernández, R.; Parsons, S.; Oswald, I. D. H.; Parkin, A.; Fabbiani, F. P. A.; Davidson, J. E.; Dawson, A.; Aird, R. E.; Jodrell, D. I.; Sadler, P. J. Structure-activity relationships for cytotoxic ruthenium(II) arene complexes containing N,N-, N,O-, and O,O-chelating ligands. *J. Med. Chem.* **2006**, *49*, 6858−6868.

(15) Cepeda, V.; Fuertes, M. A.; Castilla, J.; Alonso, C.; Quevedo, C.; Perez, J. M. Biochemical mechanisms of cisplatin cytotoxicity. *Anti-Cancer Agents Med. Chem.* **2007**, *7*, 3−18.

(16) Giaccone, G.; Herbst, R. S.; Manegold, C.; Scagliotti, G.; Rosell, R.; Miller, V.; Natale, R. B.; Schiller, J. H.; von Pawel, J.; Pluzanska, A.; et al. Gefitinib in combination with gemcitabine and cisplatin in advanced non-small-cell lung cancer: a phase III trial–INTACT 1. *J. Clin. Oncol.* **2004**, *22*, 777−784.

(17) Li, Y.; Tan, C. P.; Zhang, W.; He, L.; Ji, L. N.; Mao, Z. W. Phosphorescent iridium(III)-bis-N-heterocyclic carbene complexes as mitochondria-targeted theranostic and photodynamic anticancer agents. *Biomaterials* **2015**, *39*, 95−104.

(18) Su, X. X.; Wang, W. J.; Cao, Q.; Zhang, H.; Liu, B.; Ling, Y. Y.; Zhou, X. T.; Mao, Z. W. A carbonic anhydrase IX (CAIX)-anchored rhenium(I) photosensitizer evokes pyroptosis for enhanced anti-tumor immunity. *Angew. Chem., Int. Ed.* **2022**, *61*, No. e202115800.

(19) Gichumbi, J. M.; Friedrich, H. B. Half-sandwich complexes of platinum group metals (Ir, Rh, Ru and Os) and some recent biological and catalytic applications. *J. Organomet. Chem.* **2018**, *866*, 123−143.

(20) Geldmacher, Y.; Oleszak, M.; Sheldrick, W. S. Rhodium(III) and iridium(III) complexes as anticancer agents. *Inorg. Chim. Acta* **2012**, *393*, 84−102.

(21) Hartinger, C. G.; Metzler-Nolte, N.; Dyson, P. J. Challenges and opportunities in the development of organometallic anticancer drugs. *Organometallics* **2012**, *31*, 5677−5685.

(22) Konkankit, C. C.; Marker, S. C.; Knopf, K. M.; Wilson, J. J.; Knopf; Kevin, M.; Wilson; Justin, J. Anticancer activity of complexes of the third row transition metals, rhenium, osmium, and iridium. *Dalton Trans.* **2018**, *47*, 9934−9974.

(23) Romero-Canelón, I.; Sadler, P. J. Next-generation metal anticancer complexes: multitargeting via redox modulation. *Inorg. Chem.* **2013**, *52*, 12276−12291.

(24) Leung, C. H.; Zhong, H. J.; Chan, S. H.; Ma, D. L. Bioactive iridium and rhodium complexes as therapeutic agents. *Coord. Chem. Rev.* **2013**, *257*, 1764−1776.

(25) Dorcier, A.; Ang, W. H.; Bolaño, S.; Gonsalvi, L.; Juillerat-Jeannerat, L.; Laurenczy, G.; Peruzzini, M.; Phillips, A. D.; Zanobini, F.; Dyson, P. J. In vitro evaluation of rhodium and osmium RAPTA analogues: the case for organometallic anticancer drugs not based on ruthenium. *Organometallics* **2006**, *25*, 4090−4096.

(26) Almodares, Z.; Lucas, S. J.; Crossley, B. D.; Basri, A. M.; Pask, C. M.; Hebden, A. J.; Phillips, R. M.; Mcgowan, P. C. Rhodium, iridium, and ruthenium half-sandwich picolinamide complexes as anticancer agents. *Inorg. Chem.* **2014**, *53*, 727−736.

(27) Liu, Z.; Sadler, P. J. Organoiridium complexes: anticancer agents and catalysts. *Acc. Chem. Res.* **2014**, *47*, 1174−1185.

(28) Rono, C. K.; Chu, W. K.; Darkwa, J.; Meyer, D.; Makhubela, B. C. E. Triazolyl Ru^{II}, Rh^{III}, Os^{II}, and Ir^{III} Complexes as Potential Anticancer Agents: Synthesis, Structure Elucidation, Cytotoxicity, and DNA Model Interaction Studies. *Organometallics* **2019**, *38*, 3197−3211.

(29) Mukhopadhyay, S.; Gupta, R. K.; Paitandi, R. P.; Rana, N. K.; Sharma, G.; Koch, B.; Rana, L. K.; Hundal, M. S.; Pandey, D. S. Synthesis, structure, DNA/protein binding, and anticancer activity of some half-sandwich cyclometalated Rh(III) and Ir(III) complexes. *Organometallics* **2015**, *34*, 4491−4506.

(30) Truong, D.; Sullivan, M. P.; Tong, K. K. H.; Steel, T. R.; Prause, A.; Lovett, J. H.; Andersen, J. W.; Jamieson, S. M.; Harris, H. H.; Ott, I.; et al. Potent inhibition of thioredoxin reductase by the Rh derivatives of anticancer $M(arene/Cp^*)(NHC)Cl_2$ complexes. *Inorg. Chem.* **2020**, *59*, 3281−3289.

(31) Gupta, G.; Kumari, P.; Ryu, J. Y.; Lee, J.; Mobin, S. M.; Lee, C. Y. Mitochondrial localization of highly fluorescent and photostable BODIPY-based ruthenium(II), rhodium(III), and iridium(III) metal complexes. *Inorg. Chem.* **2019**, *58*, 8587−8595.
(32) Petrini, A.; Pettinari, R.; Marchetti, F.; Pettinari, C.; Therrien, B.; Galindo, A.; Scopelliti, R.; Riedel, T.; Dyson, P. J. Cytotoxic half-sandwich Rh(III) and Ir(III) β-diketonates. *Inorg. Chem.* **2017**, *56*, 13600−13612.
(33) Maji, M.; Acharya, S.; Bhattacharya, I.; Gupta, A.; Mukherjee, A. Effect of an imidazole-containing schiff base of an aromatic sulfonamide on the cytotoxic efficacy of N,N-coordinated half-sandwich ruthenium(II) p-cymene complexes. *Inorg. Chem.* **2021**, *60*, 4744−4754.
(34) Yang, Y.; Guo, L.; Tian, Z.; Ge, X.; Gong, Y.; Zheng, H.; Shi, S.; Liu, Z. Lysosome-targeted phosphine-imine half-sandwich iridium-(III) anticancer complexes: synthesis, characterization, and biological activity. *Organometallics* **2019**, *38*, 1761−1769.
(35) Ludwig, G.; Mijatovi, S.; Rancrosseddsignelovi, I.; Bulatovi, M.; Miljkovi, D.; Maksimovi-Ivani, D.; Korb, M.; Lang, H.; Steinborn, D.; Kaludrovi, G. N. Biological activity of neutral and cationic iridium(III) complexes with κP and κP,κS coordinated Ph_2PCH_2S-$(O)_x$Ph (x = 0−2) ligands. *Eur. J. Med. Chem.* **2013**, *69*, 216−222.
(36) Broomfield, L. M.; Alonso-Moreno, C.; Martin, E.; Shafir, A.; Posadas, I.; Ceña, V.; Castro-Osma, J. A. Aminophosphine ligands as a privileged platform for development of antitumoral ruthenium(II) arene complexes. *Dalton Trans.* **2017**, *46*, 16113−16125.
(37) Yang, Y. L.; Guo, L. H.; Ge, X. X.; Shi, S. P.; Gong, Y. T.; Xu, Z. S.; Zheng, X. F.; Liu, Z. Structure-activity relationships for highly potent half-sandwich organoiridium(III) anticancer complexes with ĈN-chelated ligands. *J. Inorg. Biochem.* **2019**, *191*, 1−7.
(38) Liu, Z.; Habtemariam, A.; Pizarro, A. M.; Fletcher, S. A.; Kisova, A.; Vrana, O.; Salassa, L.; Bruijnincx, P. C. A.; Clarkson, G. J.; Brabec, V.; et al. Organometallic half-sandwich iridium anticancer complexes. *J. Med. Chem.* **2011**, *54*, 3011−3026.
(39) Zhang, H.; Guo, L.; Tian, Z.; Tian, M.; Zhang, S.; Xu, Z.; Gong, P.; Zheng, X.; Zhao, J.; Liu, Z. Significant effects of counteranions on the anticancer activity of iridium(III) complexes. *Chem. Commun.* **2018**, *54*, 4421−4424.
(40) Morris, R. E.; Aird, R. E.; del Socorro Murdoch, P.; Chen, H.; Cummings, J.; Hughes, N. D.; Parsons, S.; Parkin, A.; Boyd, G.; Jodrell, D. I.; et al. Inhibition of cancer cell growth by ruthenium(II) arene complexes. *J. Med. Chem.* **2001**, *44*, 3616−3621.
(41) Li, J. J.; Guo, L. H.; Tian, Z. Z.; Tian, M.; Zhang, S. M.; Xu, K.; Qian, Y. C.; Liu, Z. Novel half-sandwich iridium(III) imino-pyridyl complexes showing remarkable in vitro anticancer activity. *Dalton Trans.* **2017**, *46*, 15520−15534.
(42) Tian, M.; Li, J. J.; Zhang, S. M.; Guo, L. H.; He, X. D.; Kong, D. L.; Zhang, H. R.; Liu, Z. Half-sandwich ruthenium(II) complexes containing N,N-chelated imino-pyridyl ligands that are selectively toxic to cancer cells. *Chem. Commun.* **2017**, *53*, 12810−12813.
(43) Tian, Z. Z.; Li, J. J.; Zhang, S. M.; Xu, Z. S.; Yang, Y. L.; Kong, D. L.; Zhang, H. R.; Ge, X. X.; Zhang, J. M.; Liu, Z. Lysosome-targeted chemotherapeutics: half-sandwich ruthenium(II) complexes that are selectively toxic to cancer cells. *Inorg. Chem.* **2018**, *57*, 10498−10502.
(44) Xu, Z. S.; Kong, D. L.; He, X. D.; Guo, L. H.; Ge, X. X.; Liu, X. C.; Zhang, H. R.; Li, J. J.; Yang, Y. L.; Liu, Z. Mitochondria-targeted half-sandwich rutheniumII diimine complexes: anticancer and antimetastasis via ROS-mediated signalling. *Inorg. Chem. Front.* **2018**, *5*, 2100−2105.
(45) Liu, Z.; Li, J. J.; Kong, D. L.; Tian, M.; Zhao, Y.; Xu, Z. S.; Gao, W. Y.; Zhou, Y. M. Dual functional half-sandwich Ru(II) complexes: lysosome-targeting probes and anticancer agents. *Eur. J. Inorg. Chem.* **2019**, *2019*, 287−294.
(46) Kong, D. L.; Guo, L. H.; Tian, M.; Zhang, S. M.; Tian, Z. Z.; Yang, H. Y.; Tian, Y.; Liu, Z. Lysosome-targeted potent half-sandwich iridium(III) α-diimine antitumor complexes. *Appl. Organomet. Chem.* **2019**, *33*, No. e4633.
(47) Hu, X.; Guo, L.; Liu, M.; Sun, M.; Zhang, Q.; Peng, H.; Zhang, F.; Liu, Z. Formation of iridium(III) and rhodium(III) amine, imine, and amido complexes based on pyridine−amine ligands: structural diversity arising from reaction conditions, substituent variation, and metal centers. *Inorg. Chem.* **2022**, *61*, 10051−10065.
(48) Zai, S.; Gao, H.; Huang, Z.; Hu, H.; Wu, H.; Wu, Q. Substituent effects of pyridine-amine nickel catalyst precursors on ethylene polymerization. *ACS Catal.* **2012**, *2*, 433−440.
(49) Gómez, J.; García-Herbosa, G.; Cuevas, J. V.; Arnáiz, A.; Carbayo, A.; Muñoz, A.; Falvello, L.; Fanwick, P. E. Diastereospecific and diastereoselective syntheses of ruthenium(II) complexes using N,N bidentate ligands aryl-pyridin-2-ylmethyl-amine $ArNH\text{-}CH_2\text{-}2\text{-}C_5H_4N$ and their oxidation to imine ligands. *Inorg. Chem.* **2006**, *45*, 2483−2493.
(50) Kuwata, S.; Ikariya, T. β-protic pyrazole and N-heterocyclic carbene complexes: synthesis, properties, and metal-ligand cooperative bifunctional catalysis. *Chem.—Eur. J.* **2011**, *17*, 3542−3556.
(51) Keene, F. R. Metal-ion promotion of the oxidative dehydrogenation of coordinated amines and alcohols. *Coord. Chem. Rev.* **1999**, *187*, 121−149.
(52) Nagashima, H.; Kondo, H.; Hayashida, T.; Yamaguchi, Y.; Gondo, M.; Masuda, S.; Miyazaki, K.; Matsubara, K.; Kirchner, K. Chemistry of coordinatively unsaturated organoruthenium amidinates as entry to homogeneous catalysis. *Coord. Chem. Rev.* **2003**, *245*, 177−190.
(53) Zamorano, A.; Rendón, N.; López-Serrano, J.; Álvarez, E.; Carmona, E. Activation of small molecules by the metal−amido bond of rhodium(III) and iridium(III) (η5-C5Me5)M-aminopyridinate complexes. *Inorg. Chem.* **2018**, *57*, 150−162.
(54) Li, Z.; Cai, B.; Zou, Y.; Zhang, D.; Liang, Y.; Zhou, Y.; Ma, Y.; Wang, X.; Shi, B.; Chen, W. K.; Liu, Y.; Zhao, X. Pyridyl-amine-functionalized donor−acceptor covalent organic frameworks for optimal photosynthesis of hydrogen peroxide. *Adv. Energy Mater.* **2025**, *15*, 2500341.
(55) Hohmann, H.; Hellquist, B.; Van Eldik, R. Kinetics and mechanism of the complex formation reactions of diaqua-(ethylenediamine)- and diaqua(tetraethylethylenediamine)palladium-(II) with the purine nucleosides adenosine and inosine. *Inorg. Chem.* **1992**, *31*, 345−351.
(56) Guo, L. H.; Li, P. W.; Li, J. X.; Gong, Y. W.; Li, X. Y.; Liu, Y. M.; Yu, K. J.; Liu, Z. Half-Sandwich iridium(III), rhodium(III), and ruthenium(ii) complexes chelating hybrid sp^2-N/sp^3-N donor ligands to achieve improved anticancer selectivity. *Inorg. Chem.* **2023**, *62*, 15118−15137.
(57) Guo, L. H.; Zhang, H. R.; Tian, M.; Tian, Z. Z.; Xu, Y. J.; Yang, Y. L.; Peng, H. W.; Liu, P.; Liu, Z. Electronic effects on reactivity and anticancer activity by half-sandwich N,N-chelated iridium(III) complexes. *New J. Chem.* **2018**, *42*, 16183−16192.
(58) Petrovic, A.; Milutinovic, M. M.; Petri, E. T.; Zivanovic, M.; Milivojevic, N.; Puchta, R.; Scheurer, A.; Korzekwa, J.; Klisuric, O. R.; Bogojeski, J. Synthesis of camphor-derived bis(pyrazolylpyridine) rhodium(III) complexes: structure-reactivity relationships and biological activity. *Inorg. Chem.* **2019**, *58*, 307−319.
(59) Thota, S.; Rodrigues, D. A.; Crans, D. C.; Barreiro, E. J. Ru(II) compounds: next-generation anticancer metallotherapeutics? *J. Med. Chem.* **2018**, *61*, 5805−5821.
(60) Selvam, P.; De, S.; Paira, P.; Kumar, S. K. A.; Kumar R, S.; Moorthy, A.; Ghosh, A.; Kuo, Y. C.; Banerjee, S.; Jenifer, S. K. In vitro studies on the selective cytotoxic effect of luminescent Ru(II)-p-cymene complexes of imidazo-pyridine and imidazo quinoline ligands. *Dalton Trans.* **2022**, *51*, 17263−17276.
(61) Kang, J.; Liu, Y.; Xie, M. X.; Li, S.; Jiang, M.; Wang, Y. D. Interactions of human serum albumin with chlorogenic acid and ferulic acid. Biochim. Biophys. *Biochim. Biophys. Acta, Gen. Subj.* **2004**, *1674*, 205−214.
(62) Abou-Zied, O. K.; Al-Shihi, O. I. K. Characterization of subdomain IIA binding site of human serum albumin in its native, unfolded, and refolded states using small molecular probes. *J. Am. Chem. Soc.* **2008**, *130*, 10793−10801.

https://doi.org/10.1021/acs.inorgchem.4c05599
Inorg. Chem. 2025, 64, 10379−10401

(63) Ding, F.; Zhao, G.; Huang, J.; Sun, Y.; Zhang, L. Fluorescence spectroscopic investigation of the interaction between chloramphenicol and lysozyme. *Eur. J. Med. Chem.* **2009**, *44*, 4083−4089.
(64) Johansson, J. S.; Eckenhoff, R. G.; Dutton, P. L. Binding of halothane to serum albumin demonstrated using tryptophan fluorescence. *Anesthesiology* **1995**, *83*, 316−324.
(65) Ruiz, J.; Vicente, C.; de Haro, C.n.; Bautista, D. Novel bis-C,N-cyclometalated iridium(III) thiosemicarbazide antitumor complexes: interactions with human serum albumin and DNA, and inhibition of cathepsin B. *Inorg. Chem.* **2013**, *52*, 974−982.
(66) He, W.; Li, Y.; Xue, C.; Hu, Z.; Chen, X.; Sheng, F. Effect of Chinese medicine alpinetin on the structure of human serum albumin. *Bioorg. Med. Chem.* **2005**, *13*, 1837−1845.
(67) Samari, F.; Hemmateenejad, B.; Shamsipur, M.; Rashidi, M.; Samouei, H. Affinity of two novel five-coordinated anticancer Pt(II) complexes to human and bovine serum albumins: a spectroscopic approach. *Inorg. Chem.* **2012**, *51*, 3454−3464.
(68) Castiñeiras, A.; Fernández-Hermida, N.; García-Santos, I.; Gómez-Rodríguez, L. Neutral NiII, PdII and PtII ONS-pincer complexes of 5-acetylbarbituric-4N-dimethylthiosemicarbazone: synthesis, characterization and properties. *Dalton Trans.* **2012**, *41*, 13486−13495.
(69) Wang, W. H.; Vellaisamy, K.; Li, G. D.; Wu, C.; Ko, C. N.; Leung, C. H.; Ma, D. L. Development of a long-lived luminescence probe for visualizing β-galactosidase in ovarian carcinoma cells. *Anal. Chem.* **2017**, *89*, 11679−11684.
(70) Yang, Y. L.; Guo, L. H.; Ge, X. X.; Tian, Z. Z.; Gong, Y. T.; Zheng, H. M.; Du, Q.; Zheng, X. F.; Liu, Z. Novel lysosome-targeted cyclometalated iridium(III) anticancer complexes containing imine-N-heterocyclic carbene ligands: Synthesis, spectroscopic properties and biological activity. *Dyes Pigments* **2019**, *161*, 119−129.
(71) Hayes, J. D.; Dinkova-Kostova, A. T.; Tew, K. D. Oxidative stress in cancer. *Cancer Cell* **2020**, *38*, 167−197.
(72) Swaminathan, S.; Deepak, R. J.; Karvembu, R. Interweaving catalysis and cancer using Ru- and Os-arene complexes to alter cellular redox state: A structure-activity relationship (SAR) review. *Coord. Chem. Rev.* **2023**, *491*, 215230.
(73) Liu, Z.; Romero-Canelón, I.; Qamar, B.; Hearn, J. M.; Habtemariam, A.; Barry, N. P. E.; Pizarro, A. M.; Clarkson, G. J.; Sadler, P. J. The potent oxidant anticancer activity of organoiridium catalysts. *Angew. Chem., Int. Ed.* **2014**, *53*, 3941−3946.
(74) Liu, Z.; Deeth, R. J.; Butler, J. S.; Habtemariam, A.; Newton, M. E.; Sadler, P. J. Reduction of quinones by NADH catalyzed by organoiridium complexes. *Angew. Chem., Int. Ed.* **2013**, *52*, 4194−4197.
(75) Betanzos-Lara, S.; Liu, Z.; Habtemariam, A.; Pizarro, A. M.; Qamar, B.; Sadler, P. J. Organometallic ruthenium and iridium transfer-hydrogenation catalysts using coenzyme NADH as a cofactor. *Angew. Chem., Int. Ed.* **2012**, *51*, 3897−3900.
(76) Li, J. J.; Guo, L. H.; Tian, Z. Z.; Zhang, S. M.; Xu, Z. S.; Han, Y. L.; Li, R. X.; Li, Y.; Liu, Z. Half-sandwich iridium and ruthenium complexes: effective tracking in cells and anticancer studies. *Inorg. Chem.* **2018**, *57*, 13552−13563.
(77) Trachootham, D.; Alexandre, J.; Huang, P. Targeting cancer cells by ROS-mediated mechanisms: a radical therapeutic approach? *Nat. Rev. Drug Discovery* **2009**, *8*, 579−591.
(78) Circu, M. L.; Aw, T. Y. Reactive oxygen species, cellular redox systems, and apoptosis. *Free Radical Biol. Med.* **2010**, *48*, 749−762.
(79) Perry, G.; Raina, A. K.; Nunomura, A.; Wataya, T.; Sayre, L. M.; Smith, M. A. How important is oxidative damage? Lessons from Alzheimer's disease. *Free Radical Biol. Med.* **2000**, *28*, 831−834.
(80) Kozieł, S.; Komarnicka, U. K.; Ziókowska, A.; Skórska-Stania, A.; Pucelik, B.; Płotek, M.; Sebastian, V.; Bieńko, A.; Stochel, G.; Kyzioł, A. Anticancer potency of novel organometallic Ir(III) complexes with phosphine derivatives of fluoroquinolones encapsulated in polymeric micelles. *Inorg. Chem. Front.* **2020**, *7*, 3386−3401.
(81) Azzopardi, M.; Farrugia, G.; Balzan, R. Cell-cycle involvement in autophagy and apoptosis in yeast. *Mech. Ageing Dev.* **2017**, *161*, 211−224.
(82) Acharya, A.; Das, I.; Chandhok, D.; Saha, T. Redox regulation in cancer A double-edged sword with therapeutic potential. *Oxid. Med. Cell. Longev.* **2010**, *3*, 23−34.
(83) Ye, Y.; Zhang, T.; Yuan, H.; Li, D.; Lou, H. X.; Fan, P. Mitochondria-targeted lupane triterpenoid derivatives and their selective apoptosis-inducing anticancer mechanisms. *J. Med. Chem.* **2017**, *60*, 6353−6363.
(84) Friedl, P.; Alexander, S. Cancer invasion and the microenvironment: plasticity and reciprocity. *Cell* **2011**, *147*, 992−1009.
(85) Valastyan, S.; Weinberg, R. A. Tumor metastasis: molecular insights and evolving paradigms. *Cell* **2011**, *147*, 275−292.
(86) Newby, A. C. Matrix metalloproteinases regulate migration, proliferation, and death of vascular smooth muscle cells by degrading matrix and non-matrix substrates. *Cardiovasc. Res.* **2006**, *69*, 614−624.
(87) Gialeli, C.; Theocharis, A. D.; Karamanos, N. K.; Karamanos, K. Roles of matrix metalloproteinases in cancer progression and their pharmacological targeting. *FEBS J.* **2011**, *278*, 16−27.
(88) Li, J. J.; Tian, M.; Tian, Z. Z.; Zhang, S. M.; Yan, C.; Shao, C. F.; Liu, Z. Half-sandwich iridium(III) and ruthenium(II) complexes containing P,P-chelating ligands. *Inorg. Chem.* **2018**, *57*, 1705−1716.
(89) Gao, J.; Guo, L. H.; Wu, Y. T.; Cheng, Y. H.; Hu, X. Y.; Liu, J. F.; Liu, Z. 16-Electron half-sandwich rhodium(III), iridium(III), and ruthenium(II) complexes as lysosome-targeted anticancer agents. *Organometallics* **2021**, *40*, 3999−4010.

https://doi.org/10.1021/acs.inorgchem.4c05599
Inorg. Chem. 2025, 64, 10379−10401